Supporting Information

Phase-selective Active Site on Ordered/Disordered Titanium Dioxide Enables Exceptional Photocatalytic Ammonia Synthesis

Jinsun Lee,‡[a,b] Xinghui Liu,‡[a,b] Ashwani Kumar,‡[a,b] Yosep Hwang,[a,b] Eunji Lee,[c] Jianmin Yu,[a,b]

Young Dok Kim,[b] Hyoyoung Lee[a,b,d,e]*

[a] Center for Integrated Nanostructure Physics (CINAP), Institute for Basic Science (IBS), 2066 Seoburo, Jangan-gu, Suwon 16419, Republic of Korea

[b] Department of Chemistry, Sungkyunkwan University, 2066 Seoburo, Jangan-gu, Suwon 16419, Republic of Korea.

[c] Department of Energy Science, Sungkyunkwan University, 2066 Seoburo, Jangan-gu, Suwon 16419, Republic of Korea.

[d] Department of Biophysics, Sungkyunkwan University, 2066 Seoburo, Jangan-gu, Suwon 16419, Republic of Korea.

[e] Creative Research Institute, Sungkyunkwan University, 2066 Seoburo, Jangan-gu, Suwon 16419, Republic of Korea.

‡ Authors contributed equally to this work.

*Corresponding author:

Prof. Hyoyoung Lee

E-mail: hyoyoung@skku.edu

Materials and Methods

Materials. Pristine P25-TiO_2 (Degussa), anatase (Sigma Aldrich), and rutile (Sigma Aldrich) TiO_2 were used. Lithium granules (1-6 mm (0.04-0.2 in) 99% (metals basis)), Sodium (in kerosene, pieces (large), ≥99.8% (sodium basis)) and $^{15}N_2$ isotope (98%) were obtained from Sigma Aldrich. Ethylenediamine (EDA, 98.0%) and concentrated hydrochloric acid (HCl) were purchased from Tokyo Chemical Industry (TCI). The water used in all experiments was 3rd de-ionized (3rd DI water). All the chemical reagents were used as received without further purification.

Preparation of disordered rutile/ordered anatase or disordered rutile (Li-A_o/R_d and Li-R_d). The selectively disordered rutile phase for Li-A_o/R_d and Li-R_d were synthesized through a mild alkali metal amine treatment following the previous study with a slight modification of the procedure. In brief, 0.28 g of Li granules was initially dissolved into 50 mL of ethylenediamine (EDA) to produce a 0.8 mmol/ml solvated electron solution, which was vigorously stirred for 30 min to prepare a dark-blue electride solution. Subsequently, 500 mg of completely dried commercial P25-TiO_2 nanocrystals (size: 20-40 nm) or single-phase rutile nanocrystal (size: ~30 nm) was added into the above solution slowly, which was further stirred for 30 min with vigorous stirring to ensure homogeneous dispersion. All procedures were performed in a perfectly sealed anhydrous condition and the reaction was conducted for 1, 3, and 7 days. After the reaction, dilute HCl solution (35%, OCI) in deionized (DI) water was slowly dropped into the mixture to quench the excess electrons and formed Li salts (LiCl). After the pH of the solution was adjusted below 7, the resultant solution was separated by centrifugation several times to completely remove chloride ion (Cl^-), Li salts, and EDA. Finally, the product was rinsed with deionized water and anhydrous ethanol several times and dried at 333 K in a vacuum oven overnight. For the control experiment, 75% of Li-R_d and 25% of A_o heterostructure was synthesized by hydrothermal reaction at 398K for 6 hr to make a junction between Li-R_d and A_o.

Preparation of disordered anatase/ordered rutile or disordered anatase (Na-A_d/R_o and Na-A_d). The selectively disordered anatase phase of Na-A_d/R_o and Na-A_d were synthesized through a mild alkali metal amine treatment following the previous study with a slight modification of the procedure. In brief, 0.23 g of sodium was initially dissolved into 50 mL of ethylenediamine (EDA) to produce a 0.2 mmol/ml solvated electron solution, which was

vigorously stirred for 60 min to prepare a dark-blue solution. Subsequently, 500 mg of completely dried P25-TiO_2 nanoparticles (size: 20-40 nm) or single-phase anatase nanocrystal (size: ~30 nm) was slowly added into the above solution, further stirred for 30 min with vigorous stirring to ensure homogeneous dispersion. All procedures were performed in a perfectly sealed anhydrous condition and the reaction was conducted for 1, 3, and 7 days. The purification steps were the same as in the above method for Li-A_o/R_d and Li-R_d. For the control experiment, different ratio of Na-A_d and R_o phase on Na-A_d/R_o samples (90% Na-A_d: 10% R_o and 50% Na-A_d: 50% R_o) heterostructures were synthesized by hydrothermal reaction at 398K for 6 hr to make a heterojunction between Na-A_d and R_o via a condensation reaction.

Characterizations. The crystal structures of all catalysts including their crystal orientations were investigated using X-ray diffraction (XRD) (Rigaku Ultima Ⅳ). The elemental analysis and the valence band maximum (VBM) of the catalysts were checked by X-ray photoelectron spectroscopy (XPS) on an AESXPS instrument (ESCA2000 from VG Microtech in England) equipped with an aluminum anode (Al Kα = 1486.6 eV, C1s 284.6eV). UV-vis diffuse reflectance spectra were conducted to investigate the absorbance and the energy bandgap of solid samples using a UV−vis spectrophotometer (Jasco, V-670 in Spain, in the range of 190 to 2500 nm and $BaSO_4$ as a reference) operating at room temperature. Aberration-corrected TEM (JEM-ARM200CF, JEOL) equipped with a cold field emission source operating at an accelerating voltage of 200 kV was used to acquire the high-resolution transmission electron microscopy (HRTEM) images and corresponding selected area electron diffraction (SAED, JEOL JEM-2100F) to characterize the morphology and microstructure of the catalysts. Raman spectra were collected at an emission wavelength of 532 nm using a Renishaw RM 1000-Invia micro-Raman system. To identify the N_2 adsorption on oxygen vacant sites over various samples, N_2-saturated EPR analysis was conducted at the Korea Basic Science Institute in Seoul, Korea (Experimental Condition: Microwave frequency: 9.64 GHz; Modulation frequency: 100 kHz; Temperature: 77K and 5 K). The Brunauer-Emmett-Teller (BET) at 77K was further employed to demonstrate the physisorption of N_2 molecules on the surface of the catalysts using a Micromeritics ASAP2020. ^{1}H NMR spectra were obtained using a 400 MHz Varian spectrometer to detect the $^{14}NH_4^+$ and $^{15}NH_4^+$ products after N_2 fixation using $^{15}NH_4Cl$ as standard salt. The ion exchange chromatography (ICS-3000, Dionex) was conducted after NRR using a column type of Metrosep C 4 - 150/4.0 and for Cation - 1.7 mM HNO_3 + 0.7 mM

PDCA of eluent composition at a flow rate of 0.900 mL/ min at 8.45 MPa and for Anion- 3.2 mM Na_2CO_3 + 1 mM $NaHCO_3$ at a flow rate of 0.700 mL/ min at 10.63 MPa. Gas chromatography-mass spectrometer (YL 6900 GC/MS, YL instrument, Korea) measurements were carried out using a column-Agilent DB-WAX for $^{15}N_2$ isotope experiments. The NH_3/CO_2-Temperature Programmed Desorption (TPD) (Autochem II), Pre: He/120 °C/1 hr, Ads: NH_3/CO_2/40 °C/1 hr, Measured Flow Rate: 50.12 cm^3 STP/min was measured by Korea Research Institute of Chemical Technology in Daejeon, Korea. The N_2-TPD (Autochem II 2920 Version), Pre: He/120 °C/1 hr, Ads: N_2/He 50 cc/1 hr, Measured Flow Rate: 2.232 mmol/min, was measured by PROTECH KOREA Co., Ltd. For Photoluminescence (PL), Lab-made laser confocal microscope equipped with a 0.9 NA objective lens, spectrometer, and cooled charge-coupled device was used for confocal PL (laser: 375 nm, an acquisition time of 10 s). For TRPL measurements, the sample was excited by 375 nm laser light having the pulsed width of ~70 ps with a repetition rate of 80 MHz. The PL signal was collected by 0.9 NA object lens and then guided through an optical fiber with the core diameter of 100 μm to the photodetector (HPM-100-40, Becker-Hickl GmbH). The manufactured time-correlated single-photon counting system (Simple-Tau 150, Becker-Hikl GmbH) was used to synchronize the laser and the photodetector to obtain the time profile of PL decay.

Photocatalytic N_2 reduction reaction (NRR). The photocatalytic N_2 reduction experiments were performed in 100 mL of a double-layer glass vessel for cool water-circulating in the open condition to remove oxygen evolution by continuous N_2 purging under light illumination (1 Sun, xenon lamp, AAA class by MC science). Before the reactions, samples were fully dried at 333 K in a vacuum oven to remove residual oxygen moieties on the surface and were ground using a mortar for homogenous dispersion. Typically, each photocatalyst was dispersed in 50 mL of deionized water with 7 mL of isopropyl alcohol (14%) as a hole scavenger and ultra-sonicated to form a uniform suspension. Subsequently, the suspension was bubbled under pure N_2 gas (99.999%, flow rate: 0.3 L min^{-1}, cc) to fix N_2 molecules on the surface of the catalysts in the dark and then was irradiated by Xe lamp. After the reaction, the resulting solution was filtered using a 0.1 μm Nylon membrane syringe filter and was detected by cation exchange chromatography (ICS-3000, Dionex).

Photocatalytic H_2 evolution reaction (HER). The photocatalytic H_2 evolution experiments were carried out in a 100 mL round-bottom flask completely sealed in the N_2 atmosphere under

light illumination (1 Sun, Xenon lamp, AAA class by MC science) at ambient conditions. Before the reactions, samples were dried at 333 K in a vacuum oven to remove residual oxygen moieties on the surface and were ground enough using a mortar for fine particles. Typically, each 50 mg of the photocatalyst was dispersed in 50 mL of deionized water with 7 mL of isopropyl alcohol as a hole scavenger and ultra-sonicated upto form a uniform suspension. Then, the suspension was saturated under pure N_2 (99.999%) stirring at 450 rpm in the dark and then was irradiated by Xe lamp. After the reaction, the amount of the produced H_2 was detected by gas chromatography (GC) equipped with TCD.

Determination of apparent quantum Yield (AQE). Apparent quantum efficiency (AQE) for N_2 reduction can be calculated as below:

$$\textbf{AQE}\ (\%) = \frac{Number\ of\ reacted\ electrons}{Number\ of\ incident\ photons} \times 100 = \frac{[NH_3] \times 3 \times N_a}{\frac{Light\ absorbed\ by\ the\ photocatalyst}{The\ average\ of\ photon\ energy} \times t} \times 100\ \%$$

For the photocatalytic N_2 reduction, 3 electrons are required to produce one molecule of NH_3 based on stoichiometry. As given in the equation, [NH_3] represents the number of moles of NH_3 produced and N_a is Avogadro's number (6.022 x 10^{23} mol^{-1}). The incident photon flux density is given by the light absorbed by the photocatalyst (*P* x *S*, the optical power density x irradicated area) divided by the average photon energy (hc/λ, h= the Planck's constant, and c is the velocity of light) multiplied by the irradiation time (t).

Herein, we describe the calculation for AQE of Na-A_d/R_o sample. The apparent light input (W m^{-2}) originates from the individual light intensity of bandpass filtered solar light from 500 W Xenon lamp (Monochromatic band filter: 340, 370, 400, 430, 510, 640, and 740 nm). The irradiation area (A) of the photocatalyst placed inside the photoreactor was 0.001963 m^2. The highest AQE of Na-A_d/R_o was found to be 13.6 % at 340 nm. The AQE values for other bands are given in Figure 2 g.

Spectrophotometric determination of NH_3. The concentration of the produced NH_3 was determined for $^{15}N_2$ isotope labeling experiments and Time-dependent N_2 reduction reaction on Na- A_d/R_o by the indophenol-blue method. In brief, 10 mL of the resultant solution after the

photocatalytic NRR, 0.4 mL of the phenol solution (5 g of phenol in 50 mL ethanol), and 0.4 mL of 0.5 wt% sodium nitroferricyanide were mixed. Then, 1 mL of oxidant solution (10 g of sodium citrate dihydrate, 0.5 g of sodium hydroxide, and 10 mL of sodium hypochlorite (5 %) in 50 mL of 3rd deionized water) was added into above mixture and stored in the dark for 3 h. The concentration of the product was detected using an indophenol-blue method at a wavelength of 655 nm with a UV-vis spectrometer (Jasco, V-670 in Spain, in the range of 190 to 2500 nm). The standard NH_4Cl solution at a series of concentrations was prepared to build up the calibration curves and quantify the exact amount of produced NH_3.

Spectrophotometric determination of N_2H_4. The concentration of the produced N_2H_4 was determined as a by-product by the Watt and Chrisp method. In brief, 5 mL of the resultant solution after photocatalytic NRR was collected, and 5 mL of the mixture solution (5.99 g of *p*-dimethylaminobenzaldehyde in 300 mL ethanol and 30 mLof concentrated HCl) was added. The UV-Vis absorption measurement was measured at a wavelength of 455 nm to detect the produced N_2H_4. The standard N_2H_4 solutions at a series of concentrations were prepared to build up the calibration curves and quantify the exact amount of produced N_2H_4.

Calculation method. All calculations were implemented using the Vienna Abinitio Simulation Package (VASP) code based on Density Functional Theory (DFT).[1,2] For the following calculations of properties, General gradient approximation (GGA) was used with the Perdew–Burke–Ernzerhof (PBE) functional[3] to describe the exchange-correlation potential. All structural models were entirely relaxed until the ionic Hellmann–Feynman forces were smaller than 0.001 eV/Å, the energy tolerances were less than 10^{-6} eV/atom. The interaction between core electrons and valence electrons was described using the frozen-core projector-augmented wave (PAW) method. Wave functions were expanded in a plane wave basis with high energy using plane-wave cutoff energy of 450 eV, and the corresponding gamma-centered Monkhorst-Pack[4] electronic wavevector k-point samplings were denser than 0.2 $Å^{-1}$, consistent with the previous study.[5]

The surfaces were created by starting from a bulk-relaxed (anatase and rutile) structure of TiO_2. The supercells of rutile TiO_2 was constructed by a three-layer 4×2 slab, while a three-layer 3×1 slab modeled the anatase TiO_2 (101) with a vacuum layer of 20 Å, consistent with the previous report.[5] Correspondingly, the anatase and rutile TiO_2 cluster put the two slabs based on the element ratio of XPS data, which are the initial structure of Na-A_d/R_o and Li-R_d/A_o,

respectively. Then, to approach a realistic local short-range ordered structure by following previous studies,[6,7] a fixed volume NVT ensemble has been conducted for ab-initio molecular dynamics (AIMD) to showing an analog anneal-to-quench process from 1200 to 300 K in 10 ps. Consequently, we obtain the final structure of Na-A_d/R_o (surface area 153.7 Å^2) and Li-R_d/A_o (119.2 Å^2), which will be used for further simulation. In addition, a suitable N_2 adsorption site was conducted for both heterojunctions using AIMD, suggesting that the defect site is favorable for the N_2 adsorption. Finally, the configuration of N_2 on the defect site was conducted further using AIMD simulation by fixed the catalyst at room temperature, indicating the site adopted is an active site for the study of NRR pathway (Movie S1-S6). For Gibbs free energy *(ΔG)* of the N_2 reduction steps (NRR)[8,9] is defined as below:

$$\Delta G = \Delta E_{DFT} + \Delta E_{ZPE} - T\Delta S$$

Where ΔE_{DFT} is the DFT electronic energy difference of each step, and T is the temperature (T = 298.15 K). ΔE_{ZPE} and ΔS are the difference in zero-point energy and entropy change, respectively.

In-situ diffuse reflectance infrared fourier transform spectroscopy (In-situ DRIFT) measurements. The *In-situ* DRIFT measurements were performed using a Thermo scientific, Nicolet Is10 FTIR spectrometer equipped with a diffuse reflectance accessory at the Infrared Spectroscopy. Each spectrum was recorded at a resolution of 2 cm^{-1} by averaging 128 scans. The samples were mixed with KBr powder by mortar and were held in a specimen IR reaction chamber which was specifically designed to place powder samples in diffuse reflection mode. After the chamber was sealed, pure KBr powder was first measured to obtain a background spectrum. During the *In-situ* characterization, pure N_2 gas (99.999%) and water vapor were continually introduced into the specimen chamber (flow rate 5 sccm/min). The infrared absorbance spectra were collected under dark conditions and photoirradiation using Xe lamp (500 W, solar full-spectrum). All the spectra were obtained by subtracting the background from the spectra of samples. The detailed setup is provided in supporting information.

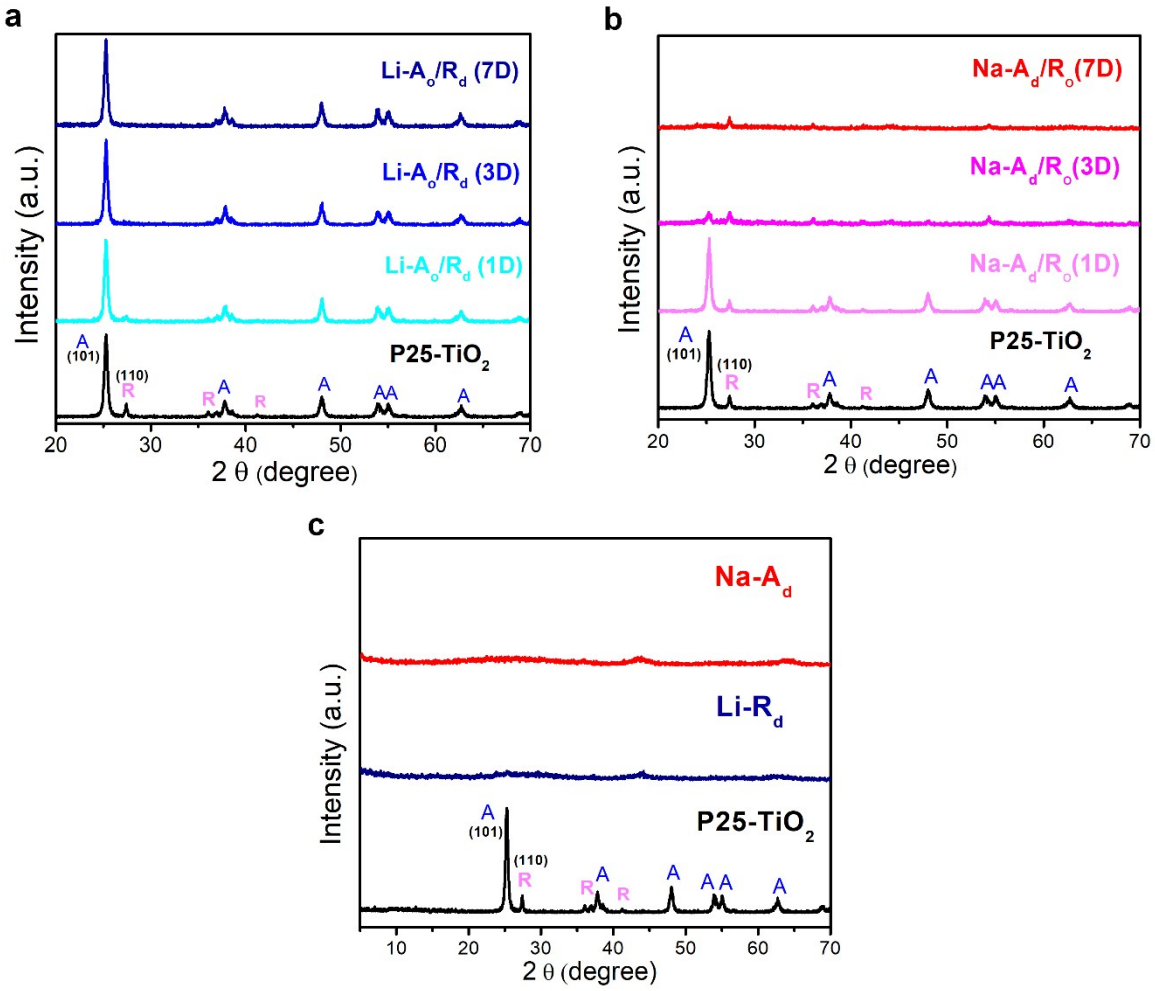

Figure S1. The powder X-ray diffraction spectra (XRD) of (a) Li-A_o/R_d, (b) Na-A_d/R_o as a function of alkali metal amine treatment time, and (c) fully reduced Li-R_d (7D) and Na-A_d (7D) compared to P25-TiO_2. (treatment time - 1D: 1 day, 3D: 3 day, 7D: 7 day).

Figure S1a,b showed a gradual reduction of R_o and A_o phases upon treatment with Li-EDA and Na-EDA, respectively. The crystal structure of R_o and A_o phases nearly disappeared after 7 days of treatment (**Figure S1c**).

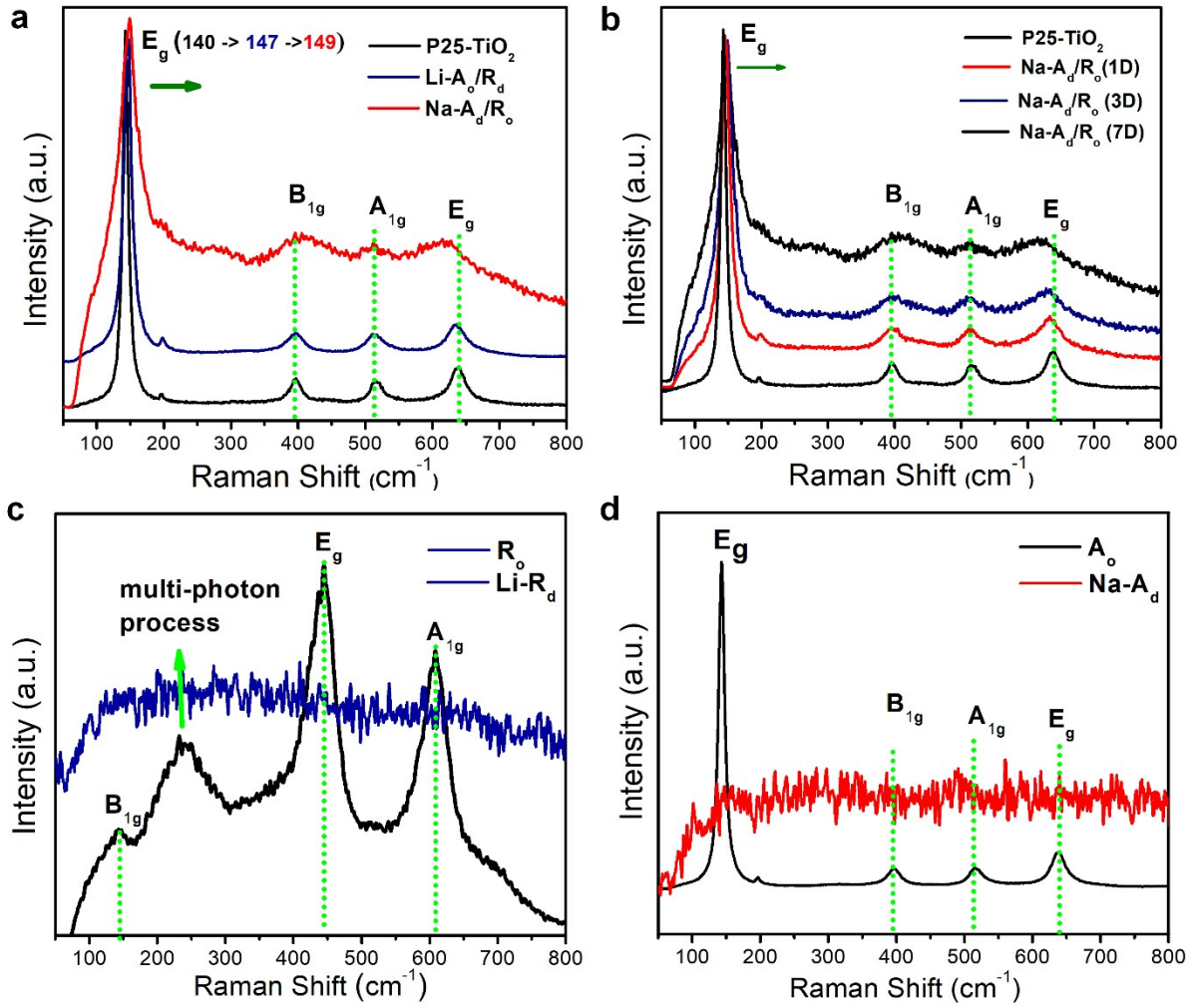

Figure S2. Raman spectra of (a) Li-A_o/R_d (7D), Na-A_d/R_o (7D) and P25-TiO_2, (b) Na-A_d/R_o with different alkali metals amine treatment time compared to P25-TiO_2. (treatment time - 1D: 1 day, 3D: 3 day, 7D:7 day). (c) Raman spectra of R_o compared to Li-R_d (7D). (d) Raman spectra of A_o compared to Na-A_d (7D).

Raman-active modes of P25-TiO_2 had four distinct bands at 140, 394, 515, and 637 cm^{-1}, which were assigned to the same E_g, B_{1g}, A_{1g}, and E_g, respectively, modes for A_o, while R_o showed three active modes (B_{1g}, E_g, A_{1g}) at 142, 449 and 609 cm^{-1}, respectively. Raman peaks of Li-A_o/R_d and Na-A_d/R_o exhibited slight upshift relative to those of P25-TiO_2, implying the gradual increase in the surface defects (oxygen vacate sites) after alkali metal amine treatment. Additionally, Raman peaks of Na-A_d/R_o and Na-A_d both decreased the intensity and increased the full width at half maximum (FWHM) attributed to a damaged crystal structure after reduction. (**Figure S2**)

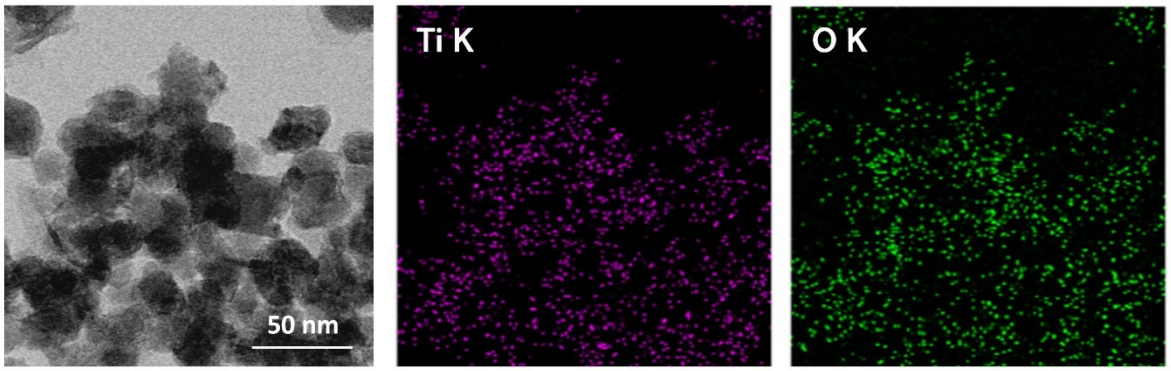

Figure S3. low magnification STEM-EDX mapping of Ti and O on Na-A_d/R_o.

Consistent with the XPS results, homogeneous distribution of Ti and O elements were observed on the nanoparticle, implying a successful synthesis of Na-A_d/R_o by alkali metal-amine treatment (**Figure S3**).

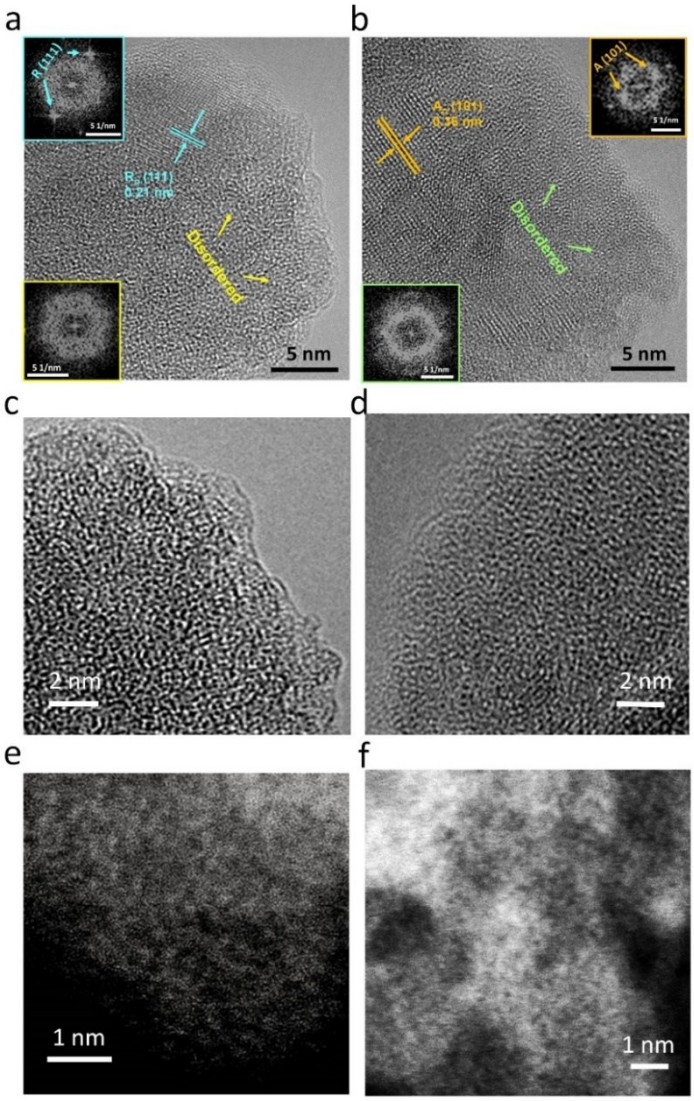

Figure S4. HR-TEM and HADDF-STEM images (a) Li-R_d (5-D treatment), (c,e) Li-R_d (7-D treatment) and (b) Na-A_d (5-D treatment), (d,f) Na-A_d (7-D treatment) via Li/Na-EDA treatments with selected-area electron diffraction.

The lattice spacing of R_o was 0.21nm for the (111) planes and 0.36 nm for the (101) planes of A_o phase TiO_2 containing an apparent amorphous layer at the edge. According to the above results, the oxygen vacant defect sites by alkali metal amine treatments occurred gradually from the edge side of the nanoparticle after 5 days of treatment (**Figure S4a,b**). After 7 days of treatment, atoms on Li-R_d and Na-A_d are randomly distributed due to disordered structure (**Figure S4c-f**)

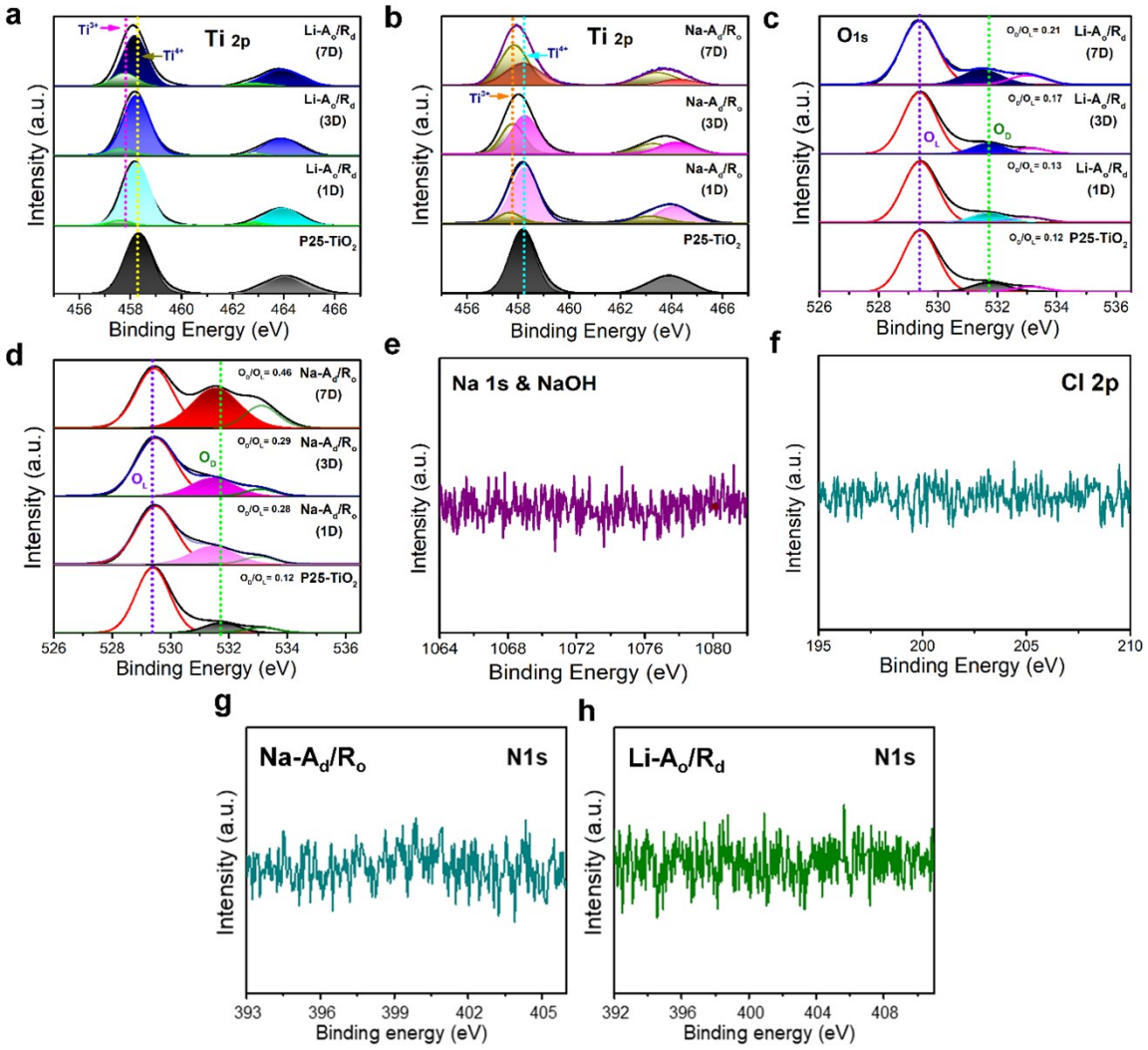

Figure S5. XPS spectra of (a) Ti 2p and (c) O 1s for Li-A_o/R_d as a function of alkali metal treatment time compared to P25-TiO_2. (treatment time - 1D: 1 day, 3D: 3 day, 7D:7 day). (b) Ti 2p and (d) O 1s for Na-A_d/R_o as a function of alkali metal treatment time compared to P25-TiO_2. (treatment time - 1D: 1 day, 3D: 3 day, 7D:7 day). (e) Na 1s & NaOH of Na-A_d and Na-A_d/R_o. and (f) Cl 2p of all samples. (g) and (h) XPS Spectra of N 1s for Li-A_o/R_d and Na-A_d/R_o.

A high-resolution XPS analysis of alkali metal amine treated samples (Li-A_o/R_d and Na-A_d/R_o) for 7D showed the number of Ti atoms with reduced charge state (Ti^{3+}), corresponding to an increase in surface Ti-OH (O_D) species at 531.4 eV as a function of reaction time (**Figure S5a-d**). Furthermore, all possible organic impurities such as alkali metal, ethylenediamine amine, and chloride were completely washed away during several purification processes (**Figure S5e-h**).

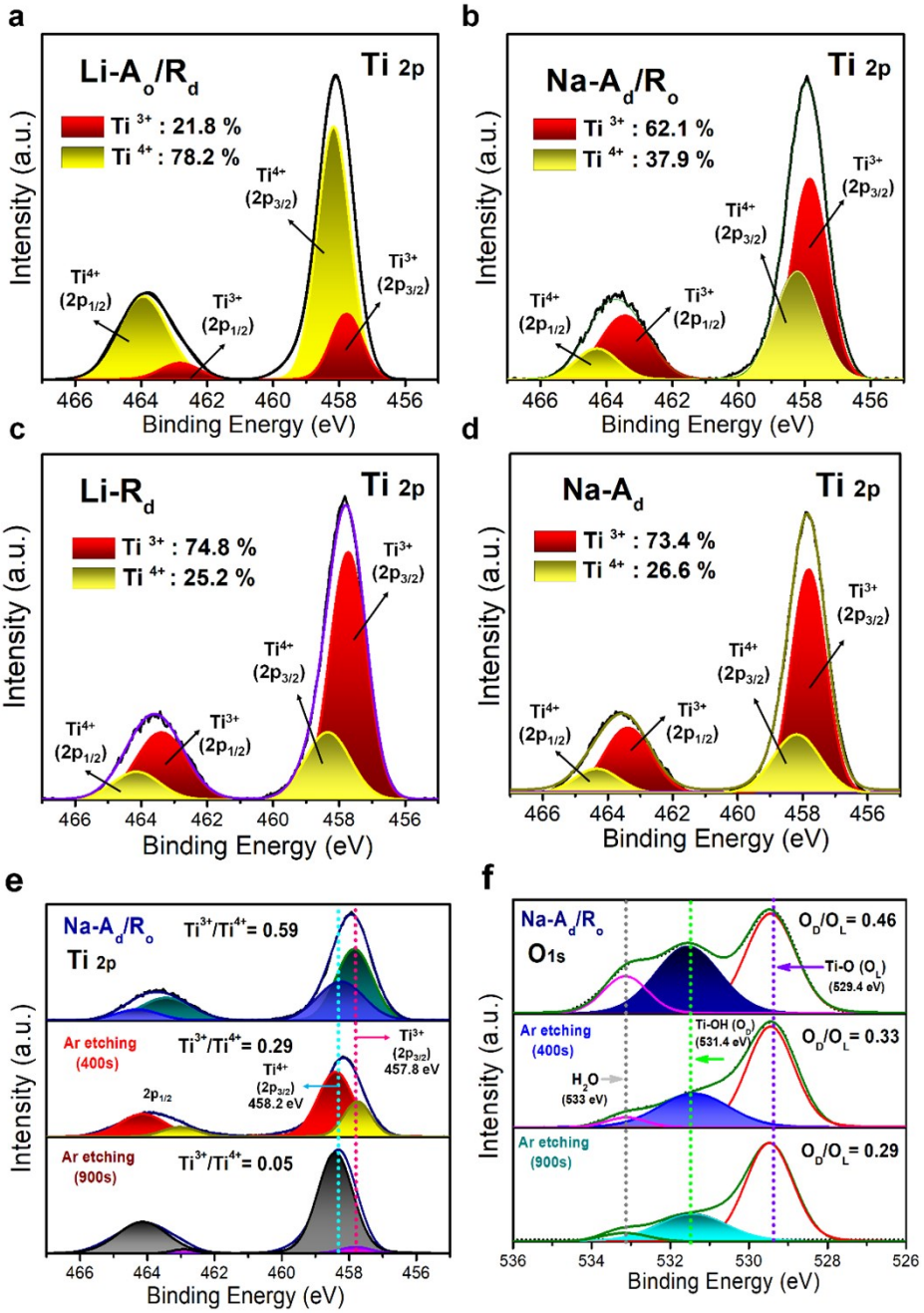

Figure S6. High-resolution XPS spectra of (a) Ti 2p for Li-A_o/R_d, (b) Na-A_d/R_o, (c) Li-R_o, and (d) Na-A_d after 7 day treatment. XPS Spectra of (e) Ti 2p and (f) O 1s for Na-A_d/R_o with different Ar etching times (0s, 400s, and 900s).

With increasing reaction time, the concentration of Ti^{3+} on the surface also increased, suggesting that the Ti^{3+} sites were mostly distributed on the surface of the TiO_2 nanoparticle. Additionally, XPS results after Ar etching showed that a ratio of Ti^{3+}/ Ti^{4+} gradually decreases from surface to core, further confirming the surface distribution of Ti^{3+} sites (**Figure S6e,f**).

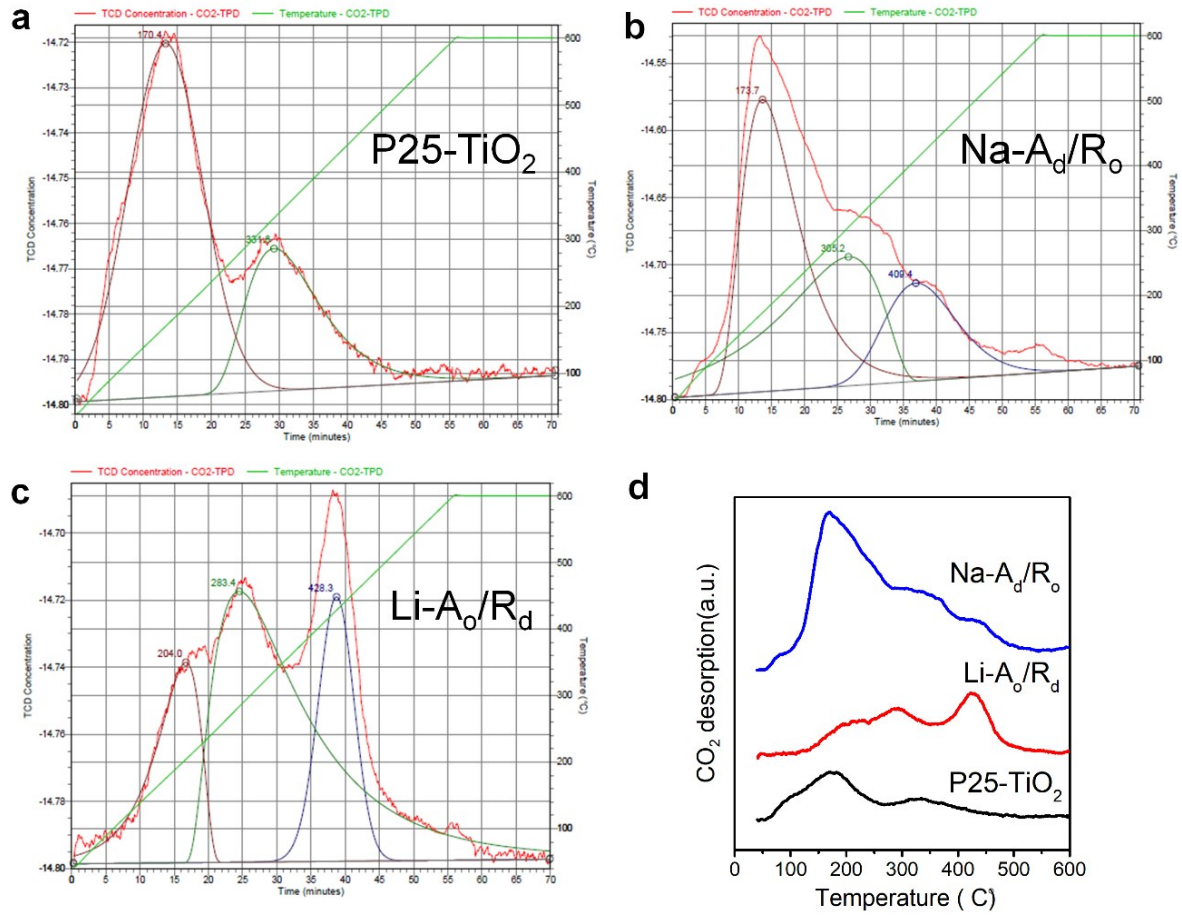

Figure S7. Profiles of CO_2 temperature-programmed desorption (CO_2-TPD) over ordered/disordered TiO_2 samples. (a) P25-TiO_2, (b) Na-A_d/R_o, (c) Li-A_o/R_d and (d) stacking plot (Pre-treatment: He/120 °C/1 h, Adsorption: CO_2/40 °C/1 hr, Measured Flow Rate: 50.12 cm^3 STP/min).

Table S1. The amount of CO_2 desorption over ordered/disordered TiO_2 samples.

Catalyst	Temperature (°C)	Quantity of desorbed CO_2 (mmol/g)	The amount of Ti^{3+} (mmol/g)
P25-TiO_2	170.4	0.22143	0.09423
	331.6	0.09423	
Li-A_o/R_d	204.0	0.09056	0.35269□
	283.4	0.26223	
	428.3	0.09046	
Na-A_d/R_o	173.7	0.51192	0.59715
	305.2	0.38697	
	409.4	0.21018	

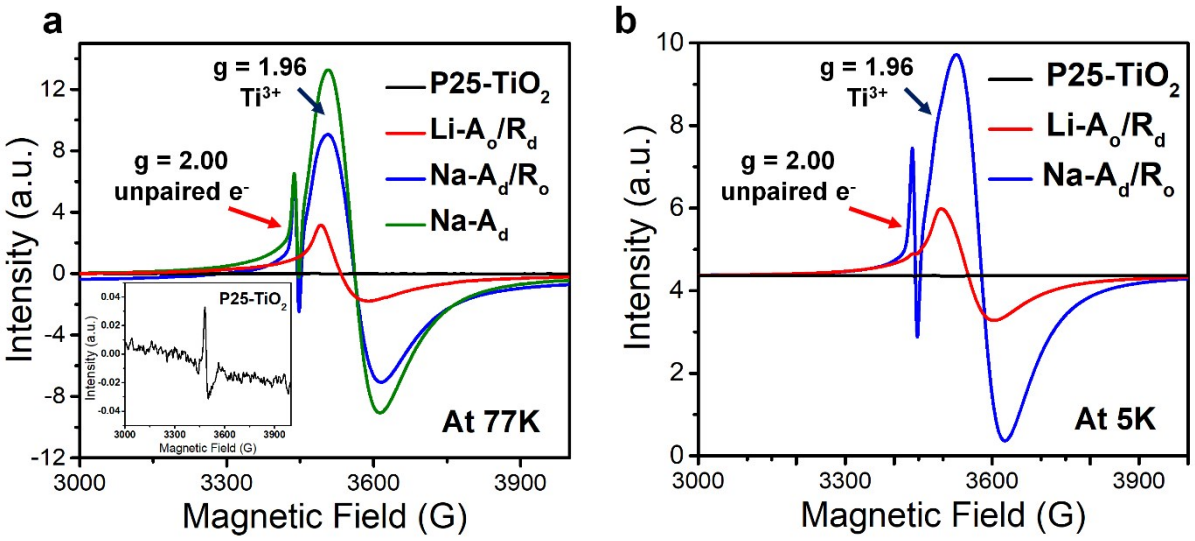

Figure S8. EPR data of (a) P25-TiO_2, Na-A_d/R_o, Li-A_o/R_d, and Na-A_d measured at 77K and (b) P25-TiO_2, Na-A_d/R_o, and Li-A_o/R_d at 5K.

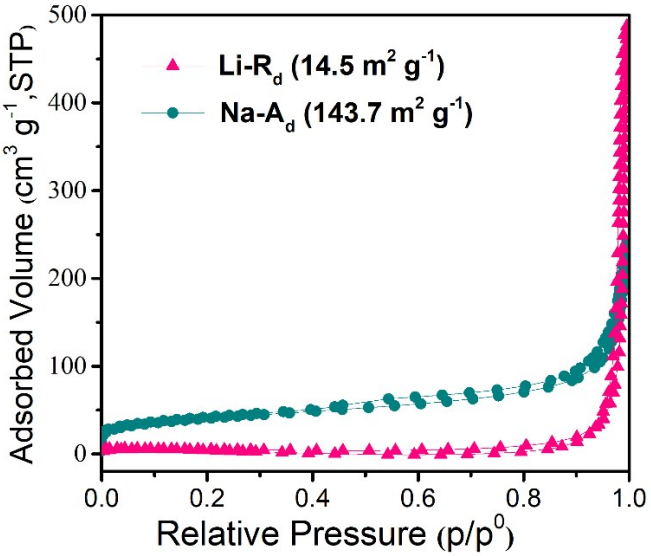

Figure S9. N_2 adsorption/desorption isotherms for Li-R_d and Na-A_d under N_2 gas as a probe molecule at 77K.

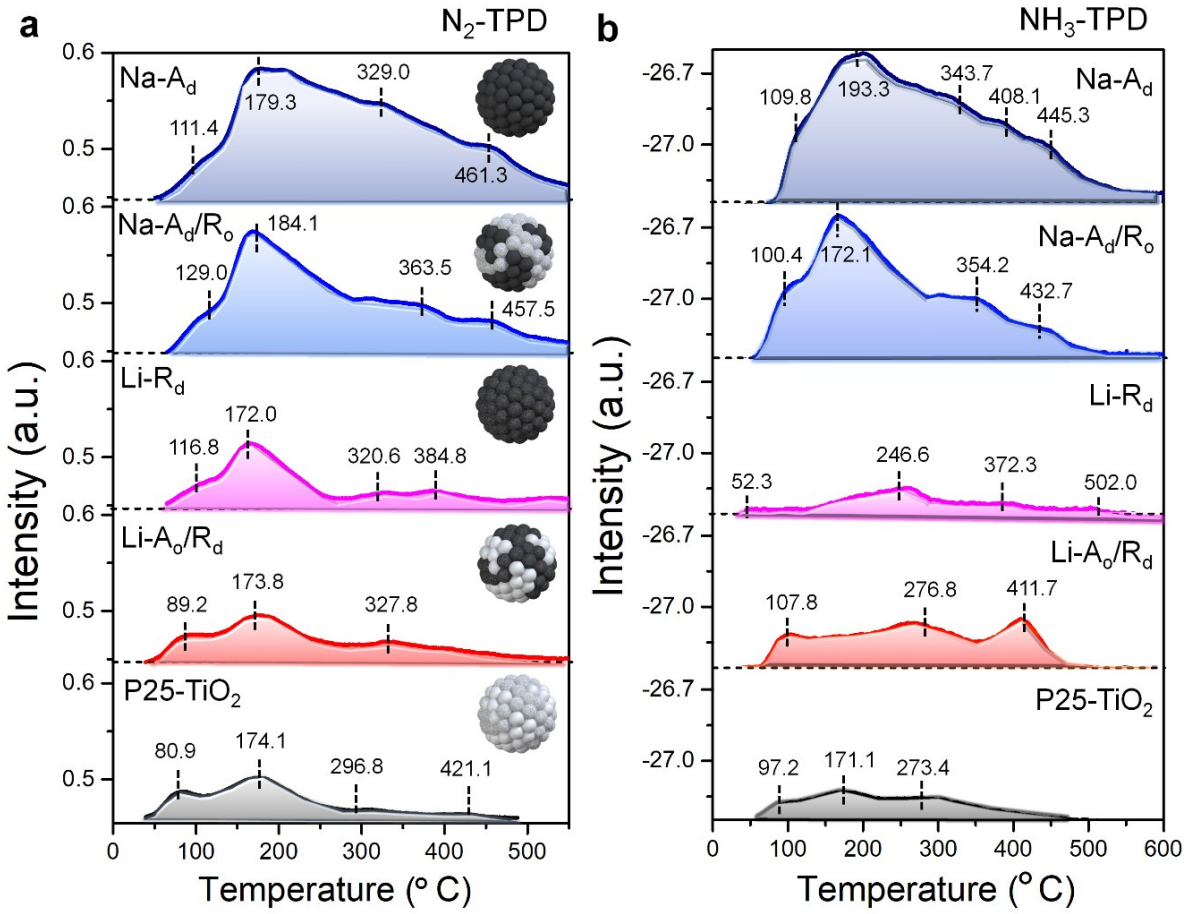

Figure S10. Profiles of Temperature-programed Desorption (TPD) of (a) N_2-TPD and (b) NH_3-TPD as a function of the desorption temperature over ordered/disordered TiO_2 samples compared to P25-TiO_2.

From a fundamental point of view, the reactant adsorption and product desorption behaviors of the solid surfaces of catalysts in a cycle are of crucial importance in N_2 reduction catalysis. Stronger N_2 chemisorption enables faster proton supply for the reaction and overcomes the activation kinetics of N_2 molecules on the catalyst surface, however, on the other side, weaker NH_3 desorption and slower release of active sites can tackle the overall reaction rate. Too strong NH_3 adsorption will lead to either active site blocking or inefficient proton supply, resulting in a sluggish N_2 reduction reaction rate.

To uncover the excellent N_2 adsorption ability on our catalysts such as a strong chemical bond, the temperature-programmed desorption of nitrogen (N_2-TPD) was characterized in **Figure S10a.** Four N_2 desorption peaks around 80-500 °C were observed on all TiO_2 series, suggesting that N_2 can be chemically adsorbed on the surface of catalysts.

Compared to those peaks in P25-TiO_2, all N_2 desorption peak centers of Na-A_d and Na-A_d/R_o were shifted to a higher temperature, whereas those for Li-R_d and Li-A_o/R_d were a negligible change, indicating that N_2 adsorption on Na-A_d and Na-A_d/R_o was stronger than Li-R_d and Li-A_o/R_d. The enhanced and selective active sites of N_2 molecules on the Na-A_d can facilitate its higher N_2 fixation.

For monitoring the NH_3 desorption behaviors and concentrations over all disordered TiO_2 catalysts were also evaluated in **Figure S10b.** The desorption of NH_3 on Na-A_d/R_o begins at 100.4°C, after reaching a maximum at around 172°C slowly decreased with high NH_3 desorption amounts compared to the other TiO_2 samples (P25-TiO_2, Li-R_d, and Li-A_o/R_d). NH_3 on Na-A_d/R_o desorbs at a slightly lower temperature, suggesting that efficient desorption of NH_3 compared to Na-A_d, which is consistent with the results in the last step of the Gibbs free energy diagram for N_2 fixation (**Figure 1f and 5d**). From these points, balanced N_2 adsorption and NH_3 desorption behaviors are the keys to the overall N_2 reduction reaction on Na-A_d/R_o (**Table S2)**.

Table S2. Total concentrations of desorbed N_2 and NH_3 over ordered/disordered TiO_2 samples compared to P25-TiO_2.

Photocatalysts	Amount of desorbed N_2 (mmol/g)	Amount of desorbed NH_3 (mmol/g)
P25-TiO_2	0.28	0.70
Li-A_o/R_d	0.42	1.35
Li-R_d	0.41	1.25
Na-A_d/R_o	1.04	2.96
Na-A_d	1.46	3.65

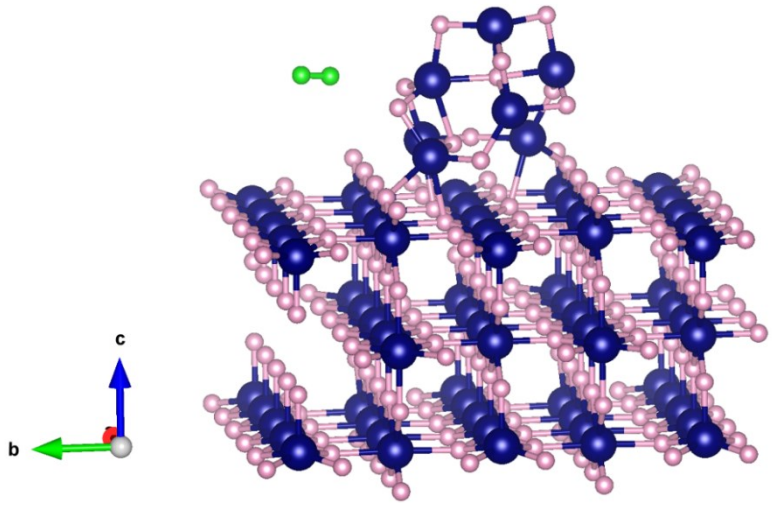

Figure S11. Optimized atomic models with N_2 molecule on Na-A_d/R_o at the heterointerface. Navy, pink, light green balls represent titanium, oxygen and nitrogen, respectively.

Note that we also checked the site N_2 adsorption at the interface site of Na-A_d/R_o (-0.024 eV); we found that the N_2 hardly adsorbed on it during the relaxation process which further proved that the active site of N_2 fixation is mainly on the Na-A_d, and the heterojunction of Na-A_d/R_o is for enhancing the interfacial charge transfer (electron/hole).

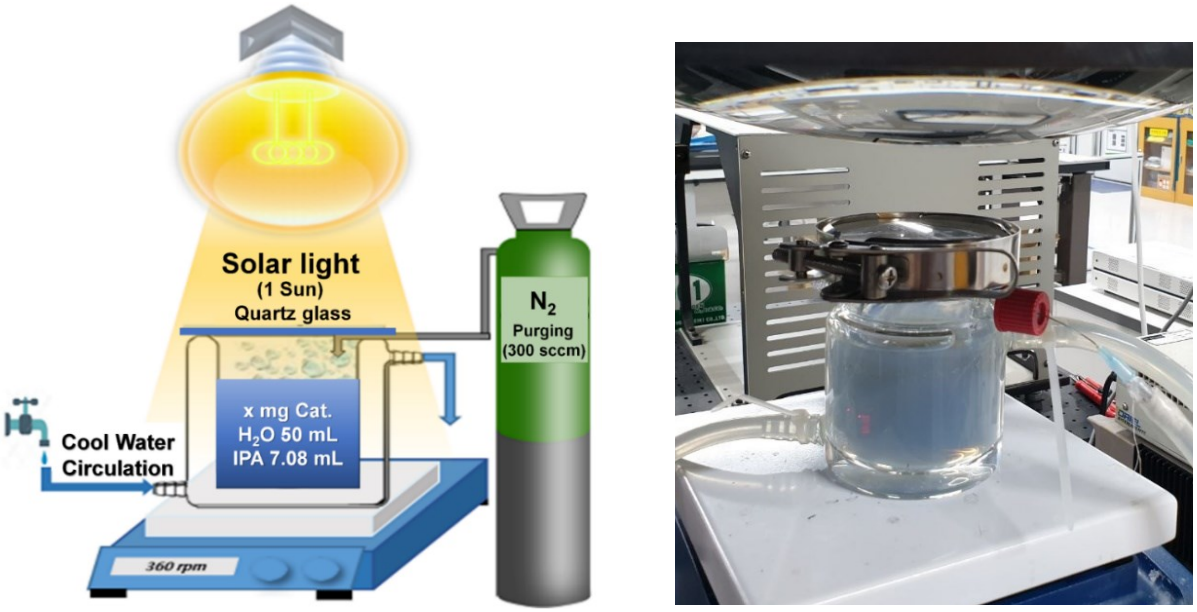

Figure S12. The setup for the N_2 reduction reaction (reaction conditions: water (50 mL), catalyst (x mg), isopropyl alcohol (7 mL), N_2 (0.3 L min $^{-1}$) under simulated AM 1.5G sunlight irradiation (1000W, Xe lamp) in a double-layered jacket with cooling water circulating line).

Table S3. Summary of the ratio of defective oxygen (O_D) species and lattice oxygen (O_L) with NH_3 yield rate on Na-R_o/A_d samples during different amine-treatment.

Na-A_d/R_o	O_D/O_L in O1s XPS	NH_3 yield rate (μmol h^{-1} g^{-1})
0 D (no treatment)	0.12	3.9
1 D	0.28	67.1
3 D	0.29	121.3
7 D	0.46	432

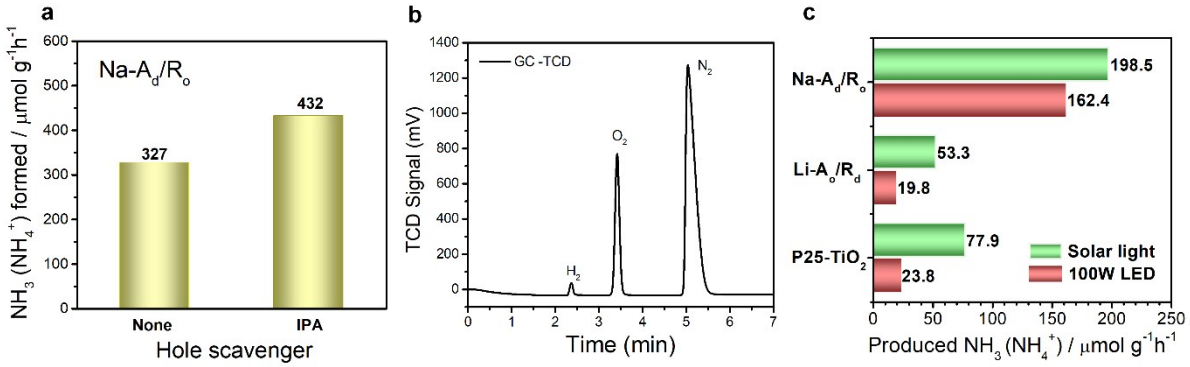

Figure S13. (a) The rate of NH_3 formation on Na-A_d/R_o in the absence and presence of a hole/hydroxyl radical scavenger under solar light irradiation. (b) Chromatogram of $H_2/O_2/N_2$ on Na-A_d/R_o after NRR for 2 h, detected by GC-TCD. (c) Nitrate anion (NO_3^-) reduction activity of P25-TiO_2, Li-A_o/R_d, and Na-A_d/R_o under full-spectrum light and visible light irradiation.

To check the amount of O_2 during NRR, we carried out NRR using Na-A_d/R_o in the N_2 saturated water without IPA for 2 h in the closed chamber, detected by GC-TCD (**Figure S13b)**. The rate of O_2 and NH_3 was 196.6 and 262.5 μmol g^{-1} h^{-1}, respectively, which is a stoichiometric ratio of NH_3 to O_2 (2: 1.5), $N_2 + 3H_2O \rightarrow 2NH_3 + 3/2O_2$. However, the amount of NH_3 was slightly less than that in the open condition. There are some probable reasons exhibiting a slightly less NH_3 synthesis and not perfectly balanced O_2 evolved:

-Not enough supply of nitrogen source during NRR. The reaction chamber has to be closed to detect the amount of oxygen, so it is not available to continuously purge the N_2 gas in the solution. Hence, most nitrogen sources existed in the gas phase and the only interface between gas and liquid phases could occur N_2 fixation.

However, even considering this point, the obtained O_2 is reasonable to explain photogenerated holes efficiently consumed via the water oxidation process on Na-A_d/R_o during NRR.

Table S4. The performance comparison of photocatalysts for N_2 fixation. (2001~2020)

S. N.	Catalyst	Reaction medium	Hole scavenger	Light Source	NH_3 yield	Φ_{AQE}	Ref.
1	**Na-A_d/R_o**	**H_2O(l), 298K, N_2**	**None**	**Solar light**	**327 μmol h^{-1} g^{-1}**	**9.2 % (λ = 340 nm)**	**This work**
2	**Na-A_d/R_o**	**H_2O(l), 298K, N_2**	**2-PrOH**	**Solar light**	**432 μmol h^{-1} g^{-1}**	**13.6 % (λ = 340 nm)**	**This work**
3	$W_{18}O_{49}$ nanowires	H_2O(l), N_2	None	Solar light	22.8 μmol L^{-1} g_{cat}^{-1} h^{-1}	9% (λ = 365 nm)	10
4	OV-BiOCl	H_2O(l), 298K, N_2	MeOH	Solar light	92.4 μmol $h^{-1}g_{cat}^{-1}$	4.3% (λ = 254 nm)	11
5	TiO_2/$SrTiO_3$/ g-C_3N_4 nanofibers	H_2O(l), 298K, N_2	10 vol% methanol	Solar light	2192 μmol g^{-1} h^{-1} L^{-1}	3.03% (λ = 365 nm)	12
6	Gd-IHEP-8 (MOFs)	H_2O(l), 298K, N_2	None	Solar light	220 μmol h^{-1} g^{-1}	2.25 % (λ = 365 nm)	13
7	R-340, TiO_2	H_2O(l), RT, N_2	10 vol% methanol	Solar light	324.9 μmol h^{-1} g^{-1}	1.1% (λ = 365 nm)	14
8	H-BiOBr	H_2O(l), 300 K, N_2	None	Solar light	360.8 μmol h^{-1}	2.11% (λ = 380 nm)	15
9	JRC-TIO-6 (TiO_2-Rutile)	H_2O(l), 313K, N_2	2-PrOH	Solar light	2.5 μM h^{-1}	0.7 % (λ < 365 nm)	16
10	WS_2@TiO_2	H2O(l), N2	0.01 M Na_2SO_3	Solar light	1.39 mmol g^{-1} h^{-1}	NA	17
11	B-doping g-C_3N_4 nanosheets	Aqueous Na_2SO_3, 298K, N_2	Na_2SO_3	λ > 400 nm	313.9 μmol g^{-1} h^{-1}	0.64% (λ = 420 nm)	18
12	Iron titanate films (Fe/Ti = 1:1)	H_2O(l), 313K, N_2	None	λ ≥ 320 nm	0.57 μmol h^{-1} cm^{-2}	NA	19
13	Bi_5O_7Br-40	H_2O(l), 298K, N_2	None	200-800 nm	12.72 mM g^{-1} h^{-1}	NA	20
14	$AuRu_{0.31}$	H_2O(l), RT, N_2 (2atm)	None	200-800 nm	101.4 μmol g^{-1} h^{-1}	NA	21
15	TiO_2 nanosheet	H_2O(l), 300 K, N_2	None	200-800 nm	78.9 μmol h^{-1} g^{-1}	0.74% (λ = 380 nm)	22
16	0.5% Cu-ZnAl-LDH	H_2O(l), 298K, N_2	None	200-800 nm	110 μmol h^{-1} g^{-1}	1.77% (λ = 265 nm)	23
17	Au/P25–K^+	H_2O(l), 38°C, N_2	MeOH	200-800 nm	1020 μmol h^{-1} g^{-1}	0.62% (λ = 550 nm)	24

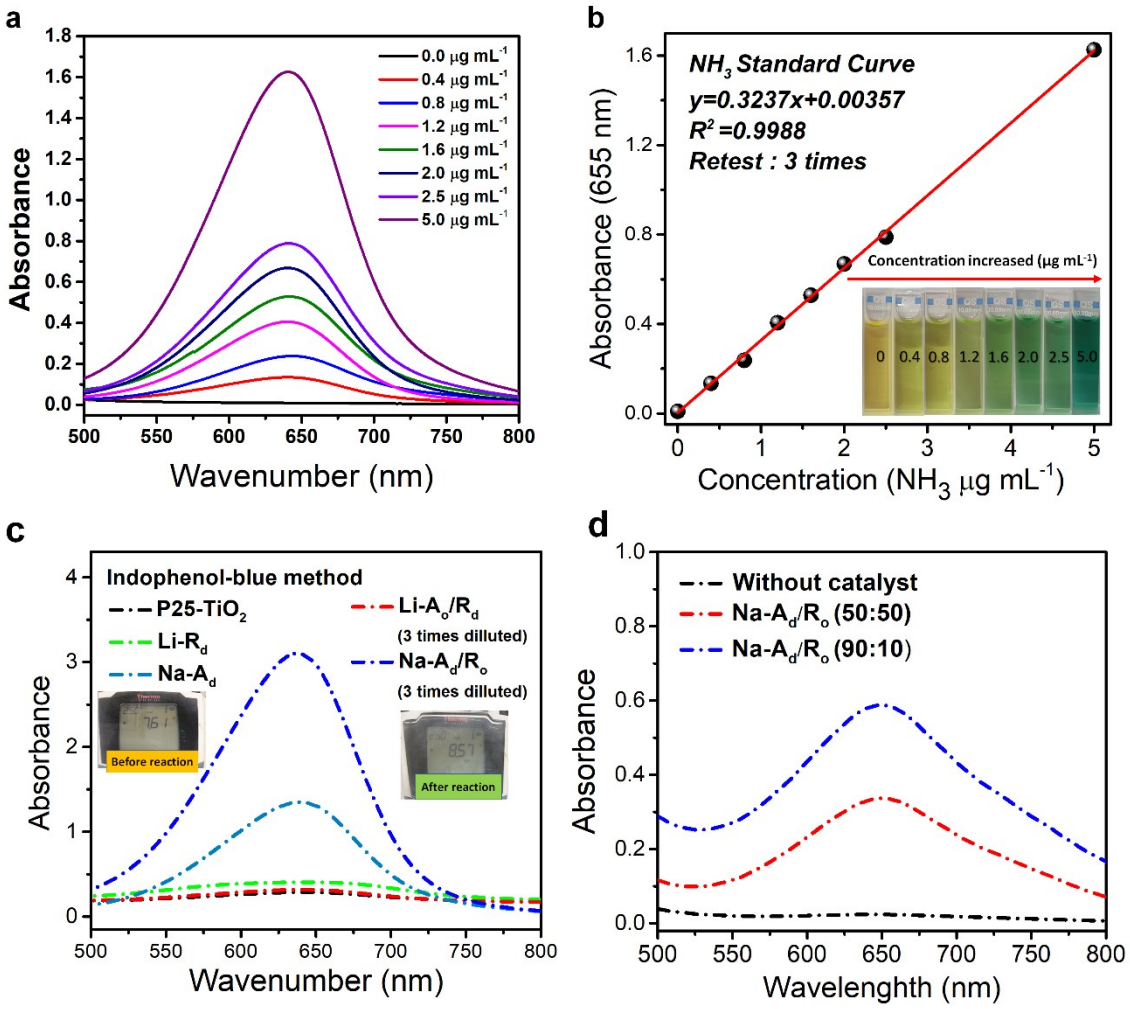

Figure S14. The colorimetric NH_3 assay calibration using the indophenol-blue method. (a) The UV-Vis absorption spectra. (b) Corresponding calibration curves. UV-vis absorption spectra of (c) ordered/disordered TiO_2 samples (inset, pH of the solution) and (d) different ratio of Na-A_d/R_o samples (Na-A_d: R_o = 90 : 10 and 50 : 50) and without catalyst after NRR detected by the indophenol-blue method.

Our reaction conditions are neutral or slight alkaline because the catalyst and solvent (water) is neutral, and IPA as hole/hydroxyl radical scavenger has a pH around 8. Hence, using the indophenol blue method for ammonia quantification in our condition is error-free, although it is used as an additional quantification method for extra evidence. (**Figure S14, inset**)

To evaluate the NRR performance over the different ratios of Na-A_d and R_o phase on Na-A_d/R_o samples (90% Na-A_d: 10% R_o and 50% Na-A_d: 50% R_o), we synthesized and checked the produced NH_3 by the indophenol blue method. According to the absorbance result, Na-A_d/R_o with 75% Na-A_d and 25% R_o (75:25) exhibited the highest NH_3 yield compared to other control ratios (90:10 and 50:50). (**Figure S14d**), suggesting that optimizing N_2 adsorption active sites on Na-A_d with a reasonable charge separation via R_o heterojunction is the key to exhibit higher NRR performances.

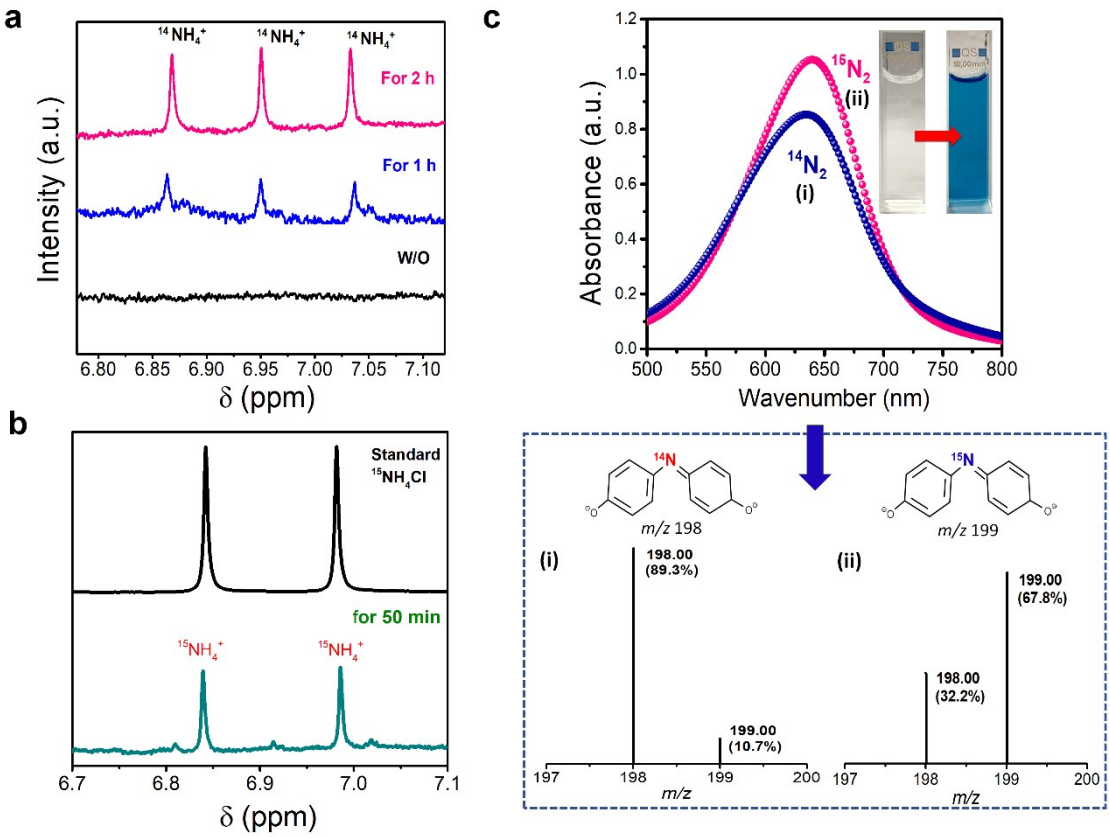

Figure S15. $^{15}N_2$ isotope labeling N_2 fixation on Na-A_d/R_o. (a) Proton NMR (400 MHz) spectra changed after photo-irradiation using $^{14}N_2$ and (b) both $^{14}N_2$ and $^{15}N_2$ gas supply as a nitrogen source. (c) UV-vis absorption spectra of the indophenol assays in the solutions after NRR under (i) $^{14}N_2$ and (ii) $^{15}N_2$ as feeding gas (top panel) and mass spectra of the respective indophenols in the solutions obtained after NRR under (i) $^{14}N_2$ and (ii) $^{15}N_2$ gas (down panel).

$^{15}N_2$ isotopic labeling experiment was conducted for NRR on Na-A_d/R_o. After 50 min at a flow rate of 8 sccm gas supply, 50 ml of solution was filtered by syringe filter and concentrated to 2 ml. Then, 0.4 ml of the resulting solution was taken out, followed by the addition 20 µl of D_2O. The obtained $^{15}NH_4$ was determined by 1H NMR spectroscopy assigned by the standard $^{5}NH_4Cl$. As seen in **Figure S15a**, the peak of $^{14}NH_4^+$ gradually increased with the increase in reaction time. When using pure $^{15}N_2$ gas as a N_2 source, only a doublet peak which corresponds to $^{15}NH_4^+$ can be found (**Figure S15b**).

The formed $^{14}NH_4^+$ and $^{15}NH_4^+$ were quantified by the indophenol-blue method, exhibiting a similar amount of NH_3 yield with $^{14}N_2$ and $^{15}N_2$ (8.2 µM, and 10.1 µM, respectively) (**Figure S15c**). Moreover, the respective solutions were examined by gas chromatography-mass spectrometry (GC-MS) analysis, assigning a clear intensity of (i) $^{14}N_2$ indophenol anion at m/z 198 after NRR under $^{14}N_2$ as feeding gas. Whereas, under $^{15}N_2$ gas, (ii) strong $^{15}N_2$ -labeled indophenol anion at m/z 199 peak with the fragment of indophenols at m/z 198, a type of chemical dissociation, in the solution. These results indicate that the N source for NH_3 truly originated from the N_2 gas.

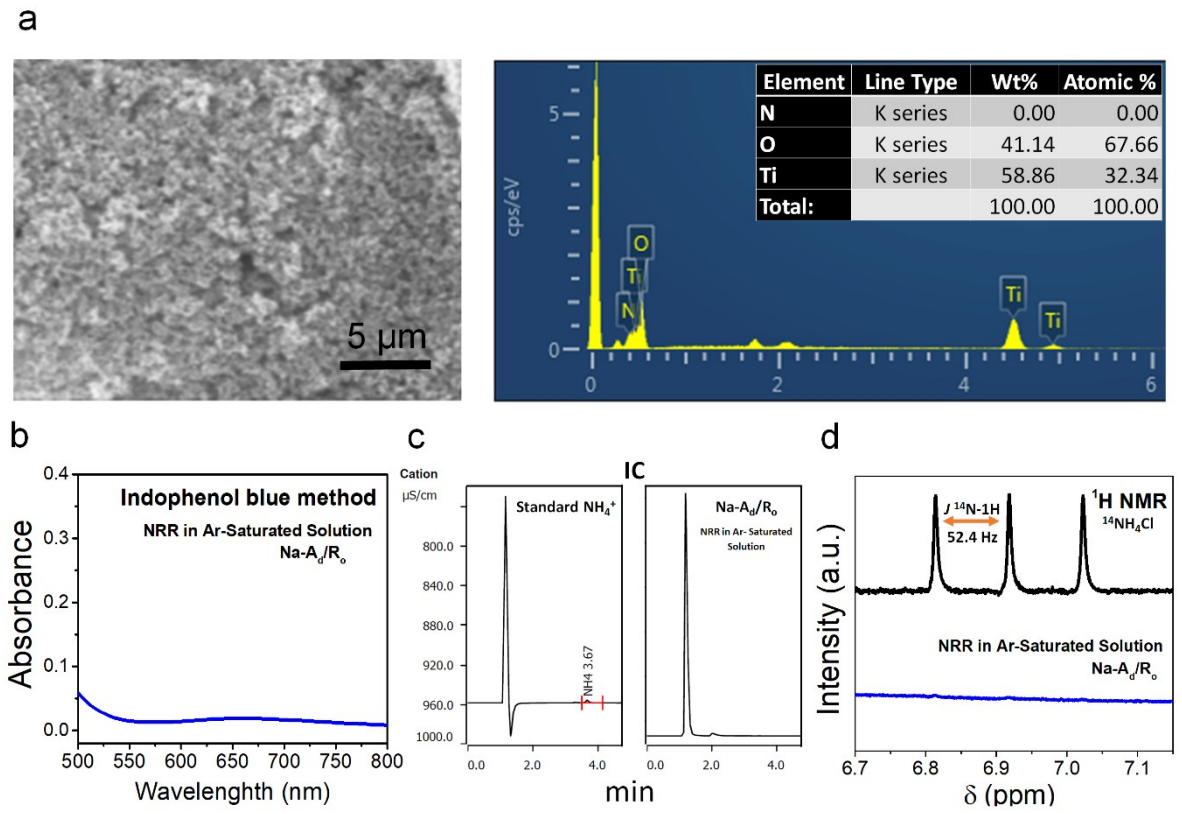

Figure S16. SEM-EDS and NH_3 quantification methods after NRR in Ar-saturated solution. (a) SEM image and EDX spectra of Na-A_d/R_o samples. The produced NH_3 was detected by (b) indophenol blue method, (c) ion chromatography (IC), and (d) ^{1}H NMR after NRR in Ar-saturated solution.

The EDX analysis (**Figure S16a)** further confirmed the absence of any N impurities from the ethylenediamine in the Na-A_d/R_o sample, suggesting a successful purification during the synthesis of catalyst, well in agreement with the N1s XPS spectra in **Figure S5g**. Additionally, we evaluated the catalytic performance of Na-A_d/R_o sample in Ar-saturated solution under a similar condition for NRR. As revealed by representative NH_3 quantification methods such as indophenol blue, IC, and ^{1}H NMR in **Figure S16b-d**, there is no NH_3 formation by Na-A_d/R_o sample under Ar-saturated solution, confirming the absence of any N source in Na-A_d/R_o sample. Therefore, the achieved NH_3 product solely resulted from the N_2 feeding gas.

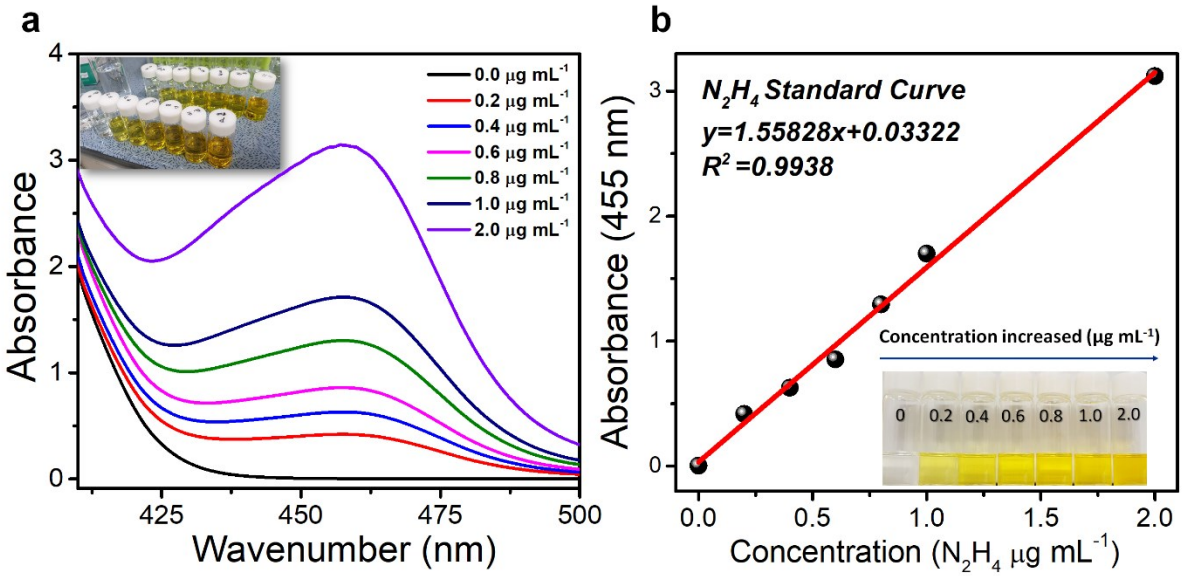

Figure S17. The colorimetric N_2H_4 assay using the Watt and Chrisps method. (a) UV-Vis absorption spectra. (b) Corresponding calibration curves.

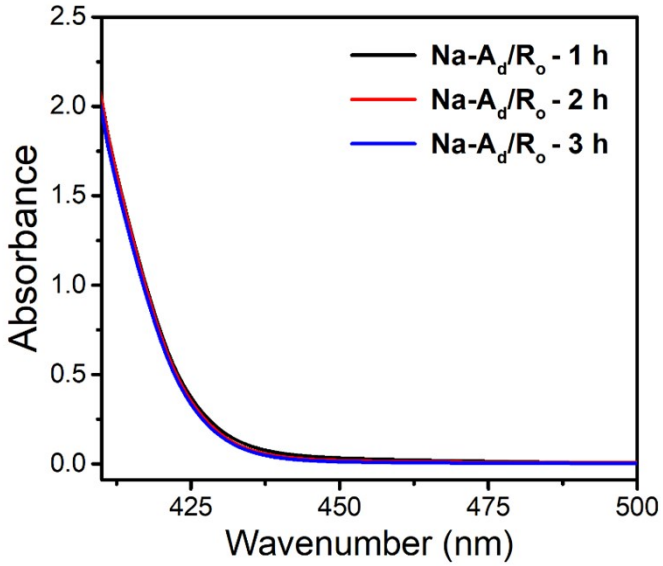

Figure S18. The UV-Vis absorption spectra for determination of the produced hydrazine using Watt and Chrisps method using Na-A_d/R_o during photocatalytic N_2 fixation.

Table S5. Summary of the produced nitrate acid (HNO_3) during NRR for various ordered/disordered TiO_2 samples detected by anion exchange chromatography (IC).

Sample	NO_3^- yield rate ($\mu mol\ h^{-1}\ g^{-1}$)
P25-TiO_2	trace
Li-A_o/R_d	trace
Na-A_d/R_o	0.17
Na-A_d	0.11
Li-R_d	trace

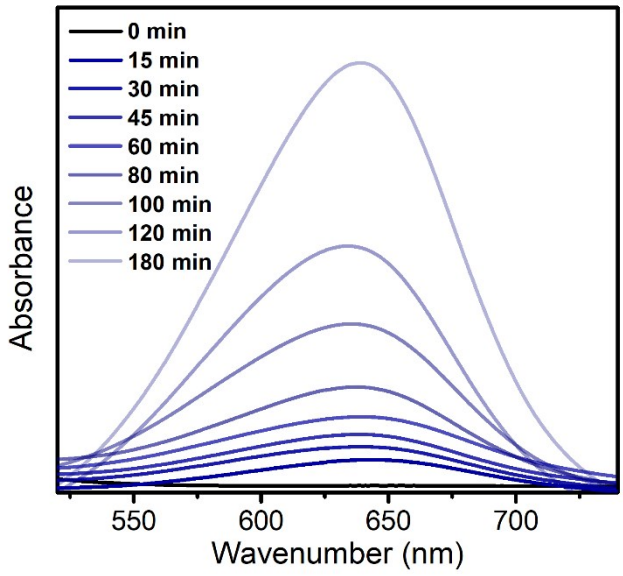

Figure S19. The UV-Vis absorption spectra of indophenol changed for Na-A_d/R_o as a function of photocatalytic N_2 fixation time.

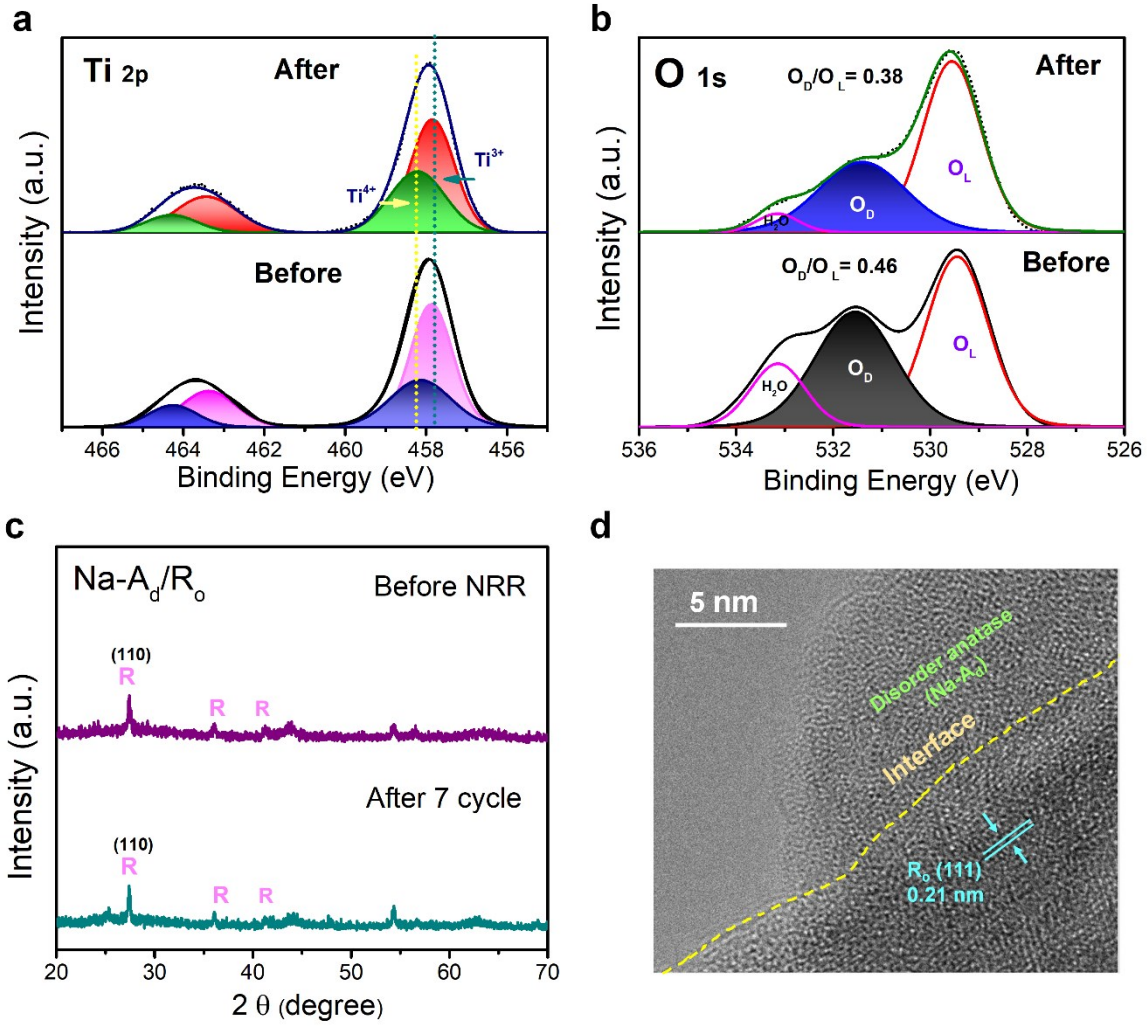

Figure S20. Examination of XPS, XRD, and TEM data of Na-A_d/R_o after N_2 fixation. XPS spectra of (a) Ti 2p and (b) O 1s for Na-A_d/R_o, respectively after cycle tests for the photocatalytic N_2 reduction reaction. (c) XRD spectra of the Na-A_d/R_o after cycle tests for the photocatalytic N_2 reduction reaction. (d) TEM image of Na- A_d/R_o at heterointerface after cycle tests for the photocatalytic N_2 reduction reaction.

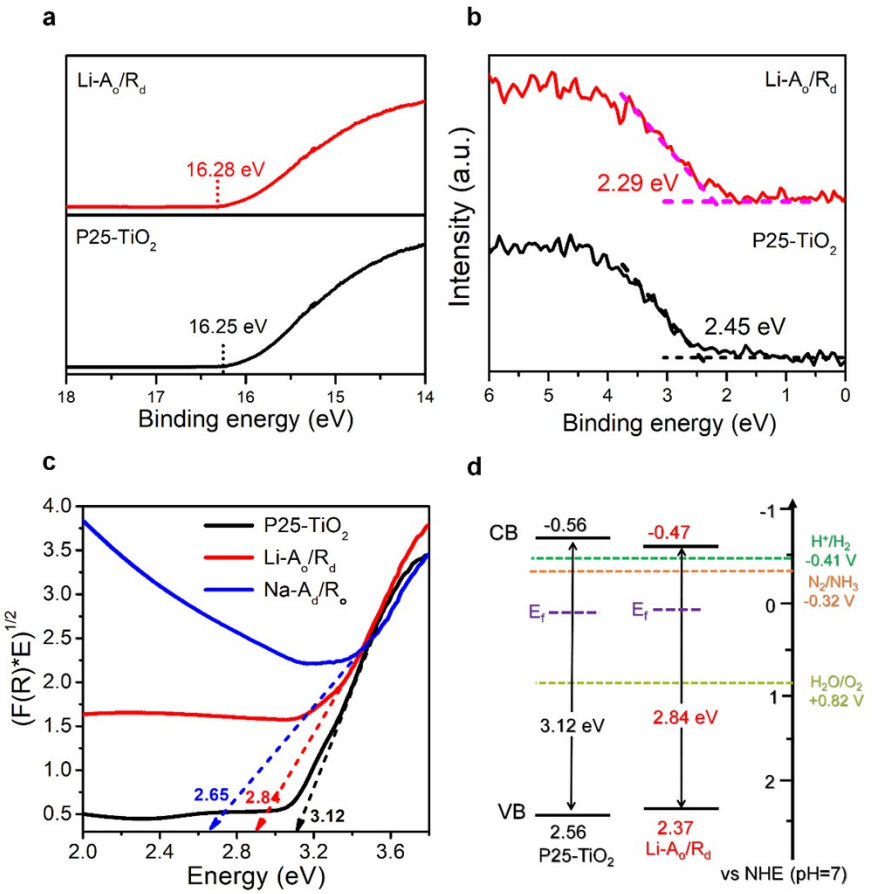

Figure S21. Spectroscopic analysis for possible charge carrier dynamics. (a) UPS spectra of P25-TiO_2, and Li-A_o/R_d. (b) Valence band XPS edge spectra of P25-TiO_2 and Li-A_o/R_d. (c) Kubelka-Munk function versus the photon energy graphs and calculated bandgap of P25-TiO_2 and Na-A_d/R_o.

Samples	A_1 (%)	τ_1 (ps)	A_2 (%)	τ_2 (ps)	τ_{av} [a](ps)
P25-TiO_2	77.8	257	22.2	2803	821.8
Na-A_d	85.2	203	14.8	1257	359.2
Na-A_d/R_o	93	139	7	788	184.3

Table S6. Kinetic analysis of PL decay over various ordered/disordered TiO_2 samples

[a] The intensity-average PL lifetime (τav) was calculated using below equation. $\tau av = (A_1\tau_1^2 + A_2\tau_2^2) / (A_1\tau_1 + A_2\tau_2)$.

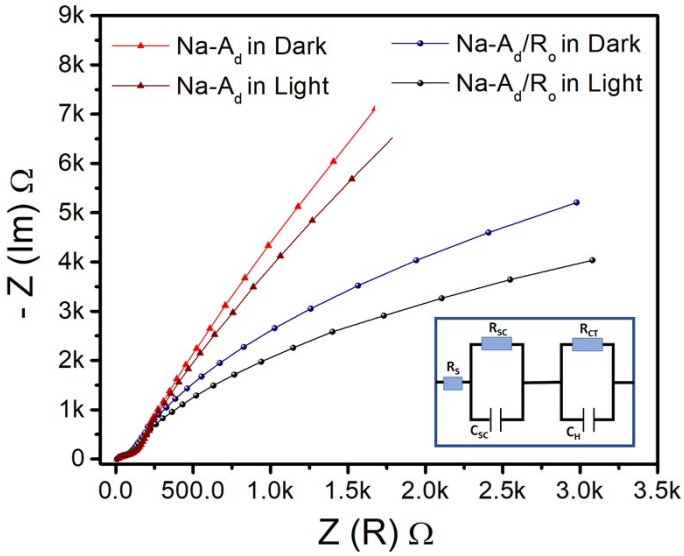

Figure S22. Charge transfer properties. EIS Nyquist plots of Na-A_d/R_o and Na-A_d in the dark and light on.

Table S7. Summary of the fitting results of impedance data for Na-A_d and Na-A_d/R_o.

	R_S (Ω)	R_{SC} (Ω)	R_{CT} (Ω)
Na-A_d in Dark	9.4	108.2	21760
Na-A_d in Light	9.4	108.6	18160
Na-A_d/R_o in Dark	9.0	79.34	9263
Na-A_d/R_o in Light	9.1	78.76	6286

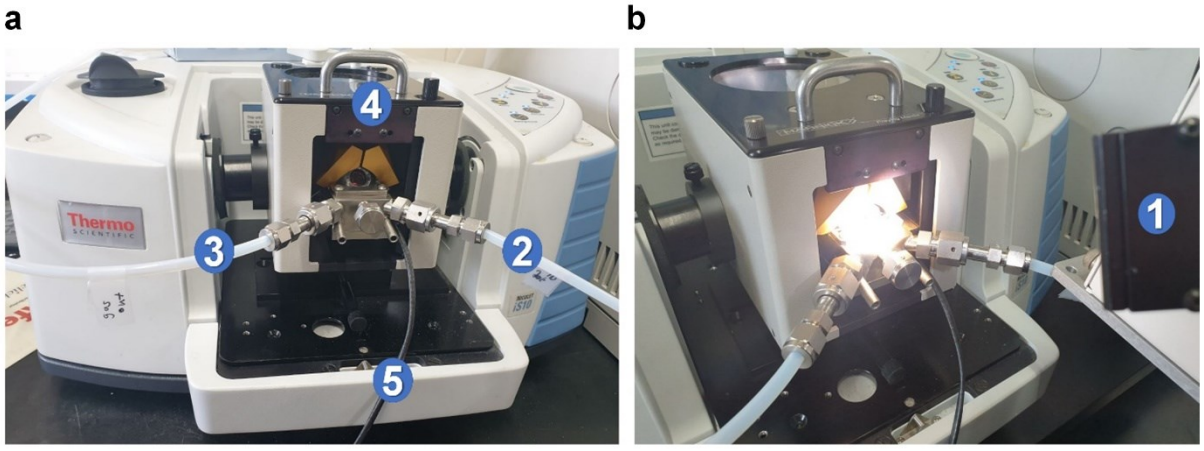

Figure S23. The photograph of the *in-situ* diffuse reflectance infrared fourier transform (*in-situ* DRIFT). (**1**. Xe Lamp; **2**. gas inlet; **3**. gas outlet; **4**. specimen chamber in *in-situ* DRIFT accessory; **5**. thermocouple) (a) light off. (b) light on.

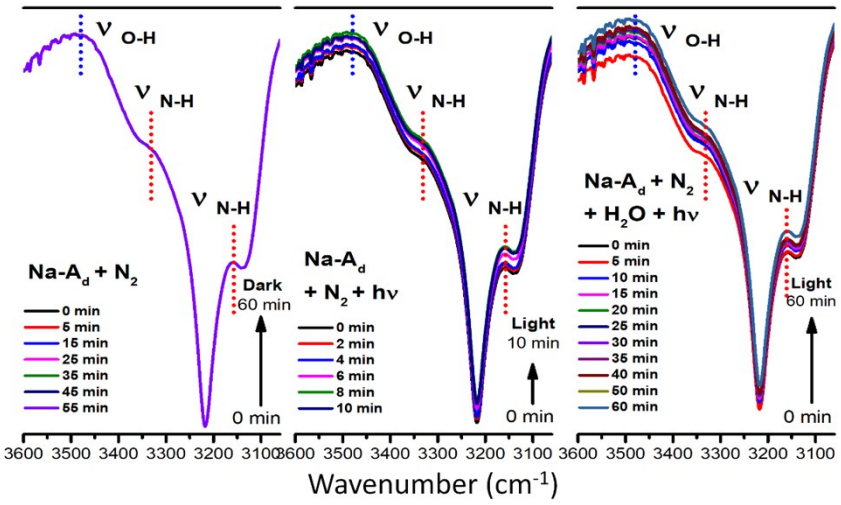

Figure S24. *In-situ* diffuse reflectance infrared fourier transform (*In-situ* DRIFT) spectra for Na-$A_{d.}$ Measurement was started in the dark with continuous N_2 gas flow to the cell, further sunlight irradiation, and water supply simultaneously (from left to right) in the gas phase at 298 K.

Similarly, the *in-situ* DRIFT spectra of Na-A_d represented a slight appearance of the N-H stretching vibration (ν_{N-H}) under solar light illumination followed by a distinguishable increase in intensity after supplying water vapor.

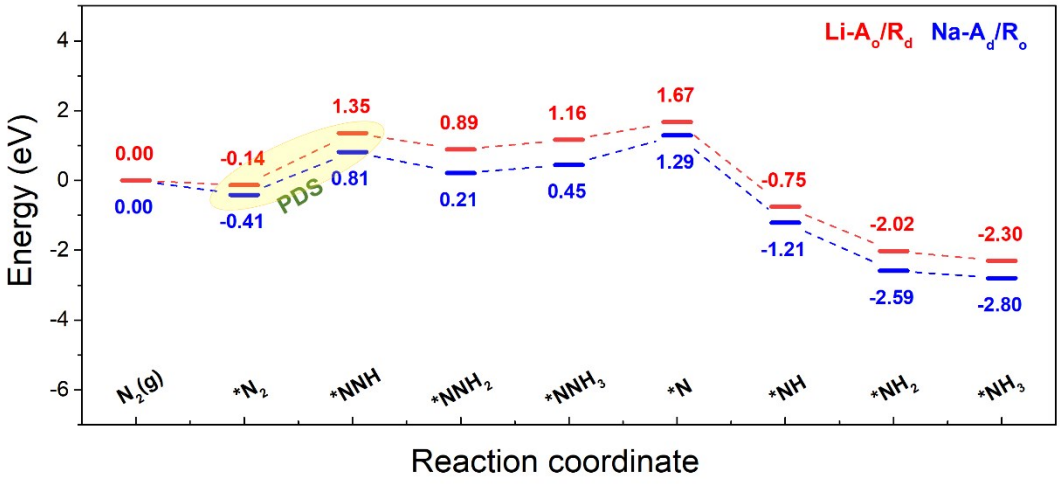

Figure S25. Gibbs free energy diagram of N_2 reduction reaction on Na-A_d/R_o and Li-A_o/R_d along the distal pathways.

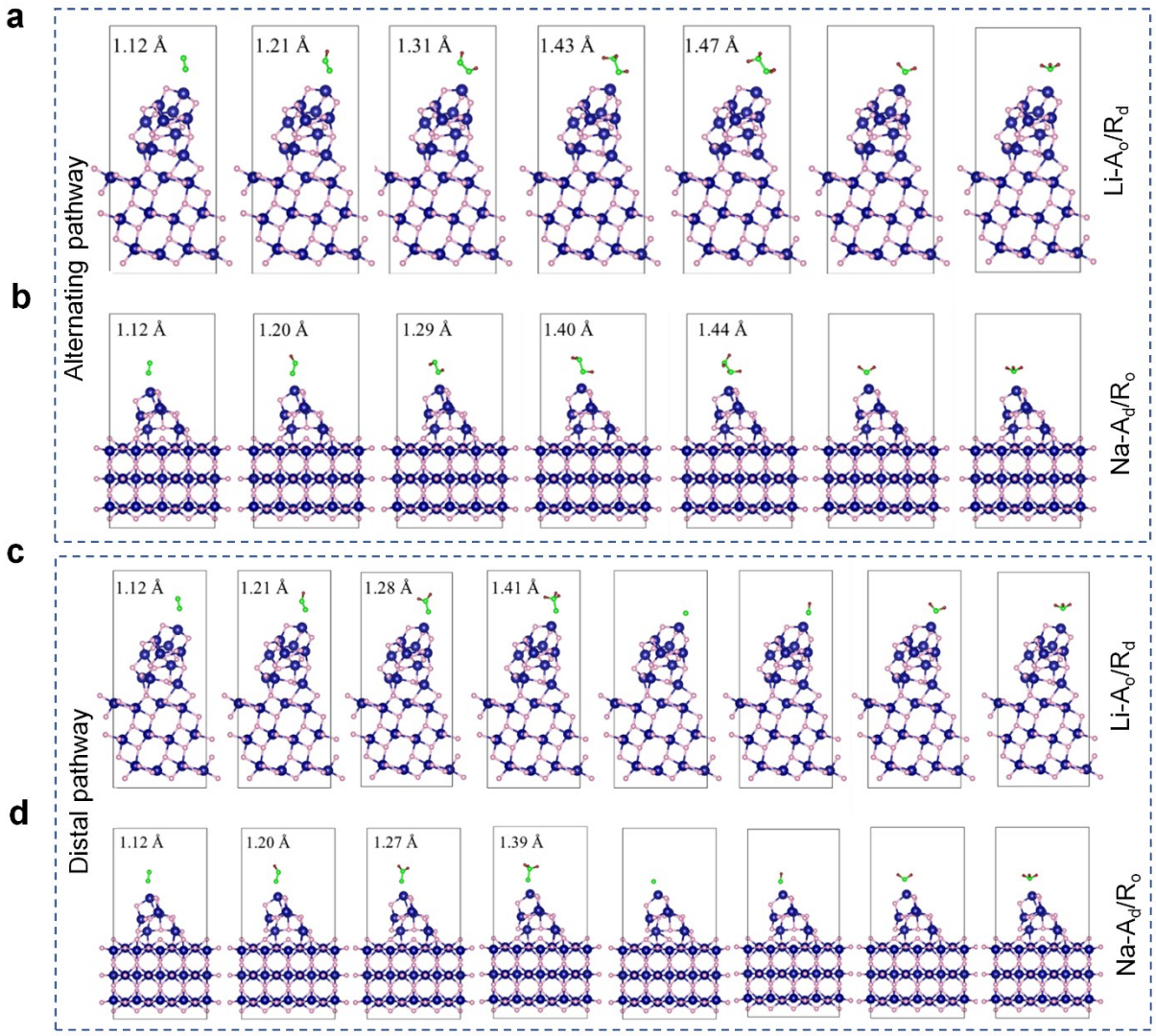

Figure S26. The optimized visual image of different steps, corresponding a) Li-A_o/R_d and b) Na-A_d/R_o for the alternating pathway and c) Li-A_o/R_d and d) Na-A_d/R_o for the distal pathway of NRR optimization. The number is the bonding length of N-N.

Discussion S1

From the reaction energy diagram of the N_2 fixation pathway of N_2 (g) → *N_2 → *NNH → *NHNH → *$NHNH_2$ → *NH_2NH_2 → *NH_2 + NH_3 →NH_3 (**Figure 5 c**), one can see that the PDS (*N2 to N–NH*) on Na-A_d/R_o was indeed favored by a lower energy barrier (1.22 eV), in comparison to 1.49 eV for Li-A_o/R_d.

Based on the DFT simulation and *In-situ* measurement, the possible photocatalytic N_2 reduction reactions on Na-A_d/R_o in water are proposed as follows:

$$N_2\,(g) + \text{Na-}A_d/R_o \rightarrow \text{Na-}A_d\text{–}{*}N_2 \quad (1)$$

$$\text{Na-}A_d/R_o + h\nu \rightarrow R_o\,(h^+) + \text{Na-}A_d\,(e^-) \quad (2)$$

$$\text{Na-}A_d\text{–}{*}N_2 + e^- + H^+ \rightarrow \text{Na-}A_d\text{–}{*}NNH \quad (3)$$

$$\text{Na-}A_d\text{–}{*}NNH + e^- + H^+ \rightarrow \text{Na-}A_d\text{–}{*}NHNH \quad (4)$$

$$\text{Na-}A_d\text{–}{*}NHNH + e^- + H^+ \rightarrow \text{Na-}A_d\text{–}{*}NHNH_2 \quad (5)$$

$$\text{Na-}A_d\text{–}{*}NHNH_2 + e^- + H^+ \rightarrow \text{Na-}A_d\text{–}{*}NH_2NH_2 \quad (6)$$

$$\text{Na-}A_d\text{–}{*}NH_2NH_2 + e^- + H^+ \rightarrow \text{Na-}A_d\text{–}{*}NH_2 + NH_3\,(g)\uparrow \quad (7)$$

$$\text{Na-}A_d\text{–}{*}NH_2 + e^- + H^+ \rightarrow \text{Na-}A_d + NH_3\,(g)\uparrow \quad (8)$$

$$3H_2O + 6R_o\,(h^+) \rightarrow 3/2O_2 + 6H^+ + 6e$$

$$N_2\,(g) + 3H_2O \rightarrow 2NH_3 + 3/2O_2 \quad \text{(Overall reaction)}$$

Supporting Movies

Movie S1
The GIF images of the optimization processes in using AMID for constructing the Li-R_d/A_o.

Movie S2
The GIF images of the optimization processes in using AMID for constructing the Na-R_o/A_d.

Movie S3
The MD simulations of N_2 adsorption sites by fixed the substrate of Li-R_d/A_o.

Movie S4
The MD simulations of N_2 adsorption sites by fixed the substrate of Na-R_o/A_d.

Movie S5
N_2 adsorption on top site (defect sites) of Li-R_d/A_o during the AIMD simulation process.

Movie S6
N_2 adsorption on top site (defect sites) of Na-R_o/A_d during the AIMD simulation process.

References

1. G. Kresse, J. Furthmüller, *Comput. Mater. Sci.,* 1996, **6**, 15– 50.

2. G. Kresse, J. Furthmuller, *Phys. Rev. B Condens. Matter.,* 1996, **54**, 11169-11186.
3. J. P. Perdew, K. Burke, M. Ernzerhof, *Physical review letters,* 1996, **77**, 3865.
4. H. J. Monkhorst, J. D. Pack, *Physical Review B,* 1976, **13**, 5188-5192.
5. K. Zhang, L. Wang, J. K. Kim, M. Ma, G. Veerappan, C.-L. Lee, K.-j. Kong, H. Lee, J.H. Park, *Energy Environ. Sci*., 2016, **9**, 499– 503.
6. J. Wang, L. Han, B. Huang, Q. Shao, H. L. Xin, X. Huang, *Nat. Commun.* **2019,** 10, 5692.
7. Y. Hu, G. Luo, L. Wang, X. Liu, Y. Qu, Y. Zhou, F. Zhou, Z. Li, Y. Li, T. Yao, C. Xion, B. Yang, Z. Yu, Y. Wu. *Adv. Energy Mater.,* 2021, **11**, 2002816.
8. E. Skúlason, T. Bligaard, S. Gudmundsdóttir, F. Studt, J. Rossmeisl, F. Abild-Pedersen, T. Vegge, H. Jónsson, J. K. A. Nørskov, *Phys. Chem. Chem. Phys*., 2021, **14**, 1235– 1245.
9. X. Guo, J. Gu, S. Lin, S. Zhang, Z. Chen, S. Huang. *J. Am. Chem. Soc.,* 2020*,* **142**, 12, 5709–5721.
10. N. Zhang, A. Jalil, D. Wu, S. Chen, Y. Liu, C. Gao, W. Ye, Z. Qi, H. Ju, C. Wang, X. Wu, L. Song, J. Zhu, Y. Xiong. *J. Am. Chem. Soc.,* 2018, **140**, 9434−9443.
11. H. Li, J. Shang, J. Shi, K. Zhao, L. Zhang. *Nanoscale,* 2016, **8**, 1986-1993.
12. R. Tao, X. Li, X. Li, C. Shao, Y. Liu. *Nanoscale*, 2020, **12**, 8320–8329.
13. K.-Q. Hu, P.-X. Qiu, L.-W. Zeng, S.-X. Hu, L. Mei, S.-W. An, Z.-W. Huang, X.-H. Kong, J.-H. Lan, J.-P. Yu, Z.-H. Zhang, Z.-F. Xu, J. K. Gibson, Z.-F. Chai, Y.-F. Bu, W.-Q. *Angew. Chem., Int. Ed.* 2020, **59**, 20666−20671.
14. G. Zhang, X. Yang, C. He, P. Zhang, H. Mi. *J. Mater. Chem. A*, 2020, **8**, 334-341.
15. Y. Bi, Y. Wang, X. Dong, N. Zheng, H. Ma, X. Zhang. *RSC Adv.,* 2018, **8**, 21871-21878.
16. H. Hirakawa, M. Hashimoto, Y. Shiraishi, T. Hirai. *J. Am. Chem. Soc.,* 2017*,* **139***,* 10929-10936.
17. L. Shi, Z. Li, L. Ju, A. Carrasco-Pena, N. Orlovskaya, H. Zhou, Y. Yang. *J. Mater. Chem. A,* 2020, **8***,* 1059−1065.
18. W. Wang, H. Zhou, Y. Liu, S. Zhang, Y. Zhang, G. Wang, H. Zhaga, H. Zhao. *Small,* 2020, **16**, 1906880.
19. O. Rusina, A. Eremenko, G. Frank, H. P. Strunk, H. Kisch. *Angew. Chem., Int. Ed.,* 2001*,* **40***,* 3993−3995.
20. P. Li, Z. Zhou, Q. Wang, M. Guo, S. W. Chen, J. X. Low, R. Long, W. Liu, P. R. Ding, Y. Y. Wu, Y. J. Xiong. *J. Am. Chem. Soc.,* 2020*,* **142***,* 12430−12439.
21. C. Hu, X. Chen, J. Jin, Y. Han, S. Chen, H. Ju, J. Cai, Y. Qiu, C. Gao, C. Wang, Z. Qi, R. Long, L. Song, Z. Liu, Y. Xiong. *J. Am. Chem. Soc.,* 2019, **141**, 7807−7814.
22. Y. Zhao, Y. Zhao, R. Shi, B. Wang, G. I. N. Waterhouse, L.-Z. Wu, C.-H. Tung, T. Zhang. *Adv. Mater.,* 2019*,* **31**, 1806482.
23. S. Zhang, Y. X. Zhao, R. Shi, C. Zhou, G. I. N. Waterhouse, L. Z. Wu, C. H. Tung, T. R. Zhang. *Adv. Energy Mater.,* 2020*,* **10***,* 1901973.
24. T.-A. Bu, Y.-C. Hao, W.-Y. Gao, X. Su, L.-W. Chen, N. Zhang, A.-X. Yin. *Nanoscale* 2019, **11***,* 10072−10079.